High Content Screening and Proteomic Analysis Identify the Kinase Inhibitor BX795 as a Potent Neuroprotective Compound in a Patient-Derived Model of Parkinson's Disease

Nasia Antoniou[1], Kanella Prodromidou[1], Georgia Kouroupi[1], Martina Samiotaki[2], George Panayotou[2], Maria Xilouri[3], Leonidas Stefanis[3, 4], Regis Grailhe[5], Era Taoufik[1*] and Rebecca Matsas[1*#]

[1]Laboratory of Cellular and Molecular Neurobiology-Stem Cells, Hellenic Pasteur Institute, 127 Vassilissis Sofias Avenue, 11521 Athens, Greece

[2]Institute of Bioinnovation, Biomedical Sciences Research Center "Alexander Fleming", Vari 16672, Greece

[3]Center of Clinical Research, Experimental Surgery and Translational Research, Biomedical Research Foundation of the Academy of Athens (BRFAA), 4 Soranou Efesiou Street, 11527 Athens, Greece

[4]1st Department of Neurology, Eginition Hospital, Medical School, National and Kapodistrian University of Athens, Athens, Greece

[5]Technology Development Platform, Screening Sciences & Novel Assay Technology, Institut Pasteur Korea, Bundang-gu, Seongnam-si, Gyeonggi-do, 463-400 Republic of Korea

*Co-senior authors

[#]Correspondence: Rebecca Matsas, Laboratory of Cellular and Molecular Neurobiology-Stem Cells, Hellenic Pasteur Institute, 127 Vassilissis Sofias Avenue, 11521 Athens, Greece; rmatsa@pasteur.gr

Abstract

Combining high throughput screening approaches with induced pluripotent stem cell (iPSC)-based disease models represents a promising unbiased strategy to identify therapies for neurodegenerative disorders. Here we applied high content imaging on iPSC-derived neurons from patients with familial Parkinson's disease bearing the G209A (p.A53T) α-synuclein (αSyn) mutation and launched a screening campaign on a small kinase inhibitor library. We thus identified the multi-kinase inhibitor BX795 that at a single dose effectively restores disease-associated neurodegenerative phenotypes. Proteomics profiling mapped the molecular pathways underlying the neuroprotective effects of BX795 that comprised a cohort of 118 protein-mediators of the core biological processes of RNA metabolism, protein synthesis, modification and clearance, and stress response, all linked to the mTORC1 signaling hub. In agreement, expression of human p.A53T-αSyn in neuron-like cells affected key components of the mTORC1 pathway resulting in aberrant protein synthesis that was restored in the presence of BX795 with concurrent facilitation of autophagy. Taken together, we have developed an adaptable platform based on p.A53T iPSC-derived neurons for drug screening and identified a promising small molecule with potent neuroprotective actions as candidate therapeutic for PD and other protein conformational disorders.

Key words

α-synuclein, p.A53T α-synuclein mutation, induced pluripotent stem cell derived neurons**,** drug screening, mTOR signaling, mRNA metabolism, proteostasis

Acknowledgements

We thank Drs. Tamotsu Yoshimori and Terje Johansen for providing GFP-LC3 and mChery-GFP-p62 plasmids, respectively. This work was supported by: a Stavros Niarchos Foundation grant to the Hellenic Pasteur Institute as part of the Foundation's initiative to support the Greek Research Center ecosystem; the Greek General Secretariat for Research and Technology grant BIOIMAGING-GR MIS 5002755 implemented under the Action "Reinforcement of Research and Innovation Infrastructure", funded by the Operational Programme "Competitiveness, Entrepreneurship and Innovation" (NSRF 2014-2020) and co-financed by Greece and the European Union (European Regional Development Fund); the Hellenic Foundation for Research and Innovation 899-PARKINSynapse grant to G.K; the National Research Foundation of Korea grant (MSIT)(NRF-2017M3A9G6068257) to RG. N.A. was recipient of a Calmette & Yersin Fellowship for a technology exchange visit to the Institut Pasteur Korea.

Data Accessibility: The mass spectrometry proteomics data have been deposited to the ProteomeXchange Consortium via the PRIDE partner repository with the dataset identifier PXD019574.

Introduction

Parkinson's disease (PD) is a complex neurodegenerative disorder affecting 2% of the world population over 65 years of age [1]. PD is characterized by motor dysfunction related to the progressive loss of midbrain dopamine neurons [2] while a wide range of non-motor symptoms are also present such as psychiatric manifestations and cognitive impairment [3]. The neuropathological hallmark of PD is the presence of intracytoplasmic inclusions in neuronal cell bodies and neurites, respectively termed Lewy bodies and Lewy neurites [4, 5]. These are protein aggregates composed mainly of α-synuclein (αSyn). αSyn is the major protein linked to sporadic PD, while point mutations and multiplications of the *SNCA* locus encoding for αSyn cause an autosomal dominant form of PD [6-8].

Despite extensive efforts in understanding PD pathogenesis, no disease modifying drugs exist. Currently only symptomatic or palliative treatments are available with none capable to prevent or slow-down disease progression. Dopamine-replacement drugs, such as Levodopa (L-dopa), which was identified 53 years ago [9], are used to ameliorate motor symptoms and remain the primary and most effective treatment despite their undesired side-effects and deterioration of efficacy with disease progression. Therefore the development of disease-modifying drugs is an urgent unmet need.

Most present-day efforts in identifying novel PD therapeutics target the aggregation of misfolded αSyn as the major pathogenic factor that causes cellular toxicity [10-13]. Alternative strategies to tackle neurodegeneration, particularly in an unbiased fashion, have lagged behind. Recent advances in patient-derived induced pluripotent stem cell (iPSC)-based models for neurodegenerative diseases permit the detection of early, potentially triggering, pathologic phenotypes and provide amenable systems for drug discovery. In combination with high throughput high content screening technologies, these approaches open new perspectives for

identification of disease-modifying compounds [14-17]. Within this context, we have previously established a robust model of iPSC-derived neurons from patients with familial PD harboring the p.A53T αSyn mutation (G209A in the *SNCA* gene) that displays disease-relevant phenotypes at basal conditions [18].Pathological features include protein aggregation, compromised neuritic outgrowth and axonal neuropathology, already evident at an early stage of neuronal differentiation [18, 19]. Because of its robustness and reproducibility, the p.A53T-model provides an ideal platform for high throughput/ high content screening approaches.

In this study, we successfully adapted this cellular system to perform the first small molecule screen on human p.A53T-neurons and discovered that the multi-kinase inhibitor BX795 significantly reverts disease-associated phenotypes. A single treatment with BX795 has sustainable effects in supporting neuritic growth, limiting αSyn protein aggregate formation and restoring axonal neuropathology in p.A53T-neurons. Strikingly, proteomics profiling by quantitative mass spectrometry revealed that treatment with BX795 results in significant downregulation of a cohort of 118 proteins that are abnormally upregulated in p.A53T-neurons. Enrichment analysis demonstrated that these proteins are predominantly associated with mRNA metabolism, mRNA transport and translation, protein metabolism and degradation processes. Using an inducible neuronal cell line expressing the human p.A53T-αSyn, we demonstrate that BX795 affects the mTORC1 pathway to restrict excessive protein synthesis and facilitate autophagy. Taken together, our data highlight the BX795 kinase inhibitor as a compelling compound and candidate therapeutic that ameliorates pathology in patient-derived p.A53T-neurons.

Results

Assay development for high content screening of p.A53T-iPSC derived neurons

iPSCs used in this study were generated from a PD patient bearing the p.A53T αSyn mutation and thoroughly characterized [18]. For directed differentiation a dual SMAD inhibition protocol was used in the presence of Noggin and TGFβ inhibitor [18, 20, 21], which favors the generation and expansion of Pax6+/Nestin+ neural progenitor cells (NPCs; Fig. 1A). NPCs were replated in neuronal differentiation medium for 7 days *in vitro* (DIV) and were allowed to further differentiate into βIII-tubulin (TUJ1)+ neurons for another two weeks (Fig. 1A). Approximately 15-20% of TUJ1+ neurons expressed the dopaminergic marker TH at this early stage (Fig. S1C). The expression of dopaminergic lineage markers, such as Nurr1, TH, and aromatic amino acid decarboxylase (AADC) was confirmed by qRT-PCR (Fig. S1A). For compound screening iPSC-derived NPCs were dissociated at DIV 7 and re-plated onto miniature 384-well plates at 9,000 cells/well, a density that was selected as the most suitable for quantitative image analysis by automated microscopy at DIV 21. As readout we assessed TH immunofluorescence, seeking to identify putative neuroprotective compounds enhancing dopaminergic neuron output. To this end, the fluorescent signal for TH within a well was normalized to the fluorescent signal for the pan-neuronal marker βIII-tubulin (TUJ1) (Fig. 1B).

High content screening of a kinase inhibitor library identifies BX795 as a compound that increases TH immunofluorescence in p.A53T-neurons

Protein kinases represent central molecular hubs that regulate numerous cell processes, thus constituting potentially attractive clinical targets. Indeed, the success of kinase inhibitors in treating cancer has spurred the evaluation of such compounds in phase II/III clinical trials as candidates for treatment of various neurodegenerative diseases [22, 23]. Since several kinases have been implicated in PD pathology [24], we screened a collection of 273 small molecule kinase inhibitors from Selleck Chemicals (Table S1) to identify molecules with prospective

neuroprotective properties. p.A53T cells adapted in 384-well plate format were exposed once (7 DIV) to the library of kinase inhibitors at 1µM concentration and quantitative image analysis was performed two weeks later, at 21 DIV (Fig. 1A). Hits were defined as compounds that robustly conferred an increase in TH expression compared to DMSO treated p.A53T neurons within a well, normalized to the expression of the pan-neuronal marker βIII-tubulin (TUJ1) (Fig. 1B). Toxic compounds were excluded by assessing cellular viability (total nuclei count) of compound-treated as compared to DMSO-treated cells (Fig. S2). From the primary screen four hits were identified (Fig. 1B), which were re-tested for validation in a dose-response assay (Fig. 1D). Of these BX795, an aminopyrimidine compound that acts as a multi-kinase inhibitor with pro-survival and/or anti-inflammatory effects [25], significantly increased TH immunofluorescence at 1 µM (Figs. 1C and D). BX-795 was initially developed as an ATP-competitive inhibitor of 3-phosphoinositide-dependent kinase 1 (PDK1), but was later shown to inhibit the IKK-related kinase, TANK-binding kinase 1 (TBK1) and IKKε, as well as to have numerous additional targets [26-28]. Based on the potent neuroprotective effect of BX795 on p.A53T dopaminergic neurons (Fig. 1D), we focused further on this compound to explore its function.

BX795 rescues neuropathological features of p.A53T neurons

The effects of BX795 on p.A53T-neurons were tested in cells that received a single treatment of the kinase inhibitor (1 µM) at 7 DIV and were analyzed two weeks later at 21 DIV, in accordance with the protocol applied during the screening procedure. In the first set of experiments a range of different drug concentrations from 0.1-2 µM was tried, including repeated drug additions every 2-3 days, with the selected scheme ensuring optimal efficacy and minimal toxicity. Initially, we asked if the enhancement in TH immunofluorescence could be attributed to an increase in cell survival/proliferation or dopaminergic differentiation in p.A53T-cultures. We could not

detect BX795-driven changes in either proliferation, as assessed by the percentage of Ki67+ cells (Fig. S1B; %ki67+ cells, DMSO: 43.3 ± 4.4, BX795: 50.3 ± 1.5, n=3), or in differentiation as estimated by the percentage of Nestin+, TUJ1+ or TH+ cells in the culture (Fig. S1C; % Nestin+ cells, DMSO: 25.3 ± 3.7, BX795: 22.3 ± 6.1, n=3; % βIII-tubulin cells, DMSO: 19.5 ± 4.2, BX795: 18.8 ± 4.4, n=4; % TH+ cells out of all TUJ1+ cells, DMSO: 13.9 ± 3.1, BX795: 18.1.0 ± 3.9, n=3). These observations indicate that the effect of BX795 on dopaminergic neurons is not related to an increase in either survival/proliferation or differentiation.

Next, we investigated if treatment with BX795 could rescue neuropathological features previously identified in p.A53T-neurons, such as compromised neuritic growth, dystrophic or fragmented neurites and the presence of intracellular protein aggregates [18, 19]. Evaluation of total neurite length in p.A53T TH+ dopaminergic neurons revealed a significant increase in response to BX795 (length in µm, DMSO: 133.8 ± 15.4, BX795: 164.0 ± 20.2, n=4, Fig.2A) compatible with the observed increase in TH immunofluorescence. Moreover, examination of the distinct pathological morphology of TUJ1+ p.A53T neurons revealed an almost 50% reduction in axonal degeneration (axon degeneration index: DMSO: 13.03 + 1.5, BX795: 7.3 + 1.0, n=3; Fig. 2B), indicating that the neuroprotective effects of the compound are not restricted to dopaminergic neurons. Finally, exposure to BX795 resulted in a significant decrease in protein aggregate formation in p.A53T cells (number of aggregates per cell, DMSO: 5.00 + 0.52, n= 88, BX795: 3.35 + 0.29, n=96; Fig. 2C) accompanied by a decline in the levels of (Ser129)-phosphorylated αSyn (Fig. 2D), a modification that renders αSyn prone to self-assembly and is commonly associated with synucleinopathy [29, 30]. The BX795 enhancement in neuritic growth and the decrease in the neurodegeneration index were also confirmed in a previously well characterized line of p.A53T-neurons from a second patient (Fig. S3) [18, 19].

Taken together our results indicate that a single treatment with BX795 exerts prominent and sustainable neuroprotection in p.A53T neurons by improving neuritic growth, limiting the levels of pathological αSyn and restricting aggregate formation whilst maintaining axonal integrity.

Proteomics analysis identifies cellular pathways targeted by BX795 in p.A53T neurons

Identification of the BX795 targets, which vary according to the system investigated [27, 28, 31], is a challenging task. To gain insight into the cellular pathways affected by BX795 we used an unbiased approach, based on comparative proteomics using LC-MS/MS and label-free quantification in p.A53T and control neurons derived from a healthy subject (wild-type SNCA) [18], treated or not with BX795. Similarly to the screening procedure, BX795 was added once at DIV 7 and proteomics analysis was performed at DIV 21 when rescue of neuropathological phenotypes was noted (Fig. 2). A total of 1652 proteins were identified and quantified using the MaxQuant software [32, 33], followed by filtering of low quality protein hits with the Perseus software. In order to identify differentially expressed proteins, we compared all experimental groups using ANOVA testing (permutation-based FDR with 0.05 cut-off). Initial comparison between p.A53T versus control neurons in the absence of BX795, revealed differential expression of 640 proteins (Fig. S4A) from which only 67 were down-regulated whilst the rest 573 were up-regulated (Fig. S4B, Table S4). This large increase in protein expression was linked by GO enrichment analysis mainly to the biological processes of transcription, translation, protein synthesis and modification (Fig. S4B). Remarkably the levels of a cohort of 118 proteins, lying mostly within these biological processes and representing approximately 20% of the total dysregulated proteins in p.A53T neurons, were restored upon treatment with BX795 ($p<0.05$) (Fig. 3A, Table S2). Most importantly, this outcome was specific to p.A53T-neurons as BX795 had no significant effect on the proteome of control neurons.

Extensive data mining by GO enrichment analysis for biological processes, molecular function and cellular compartments ($p<0.01$), complemented by reactome pathway analysis ($p<0.01$), highlighted the dysregulated core pathways in p.A53T-neurons and, amongst them, those targeted by BX795 to restore neuronal physiology (Fig. 3B). These include proteins associated with RNA metabolism, protein synthesis, protein modification and transport, stress response, and neurodegeneration, as outlined below.

RNA metabolism. The p.A53T proteome showed enrichment for proteins in subcellular compartments known to be associated with αSyn [34], including membrane bound organelles (204 proteins), mitochondria (118), ribosomal complexes (29), nucleus (292), and neuron projection/axon cytoplasm (10) (Table S3). In agreement, processes such as cellular metabolism, translational initiation and regulation, tRNA aminoacetylation and export from nucleus, mRNA stability and export from nucleus, rRNA processing, formation of pre-initiation complex and protein folding were among the top pathways enriched in the p.A53T proteome as compared to control (Fig. S4). A previous study in mouse neurons has identified mRNA binding proteins (RBPs) and those involved in protein biosynthesis within the protein network that is in immediate vicinity of αSyn, suggesting that perturbation of these pathways may be directly related to pathology [34]. Herein, we provide evidence that these same pathways are altered when p.A53T is expressed in human neurons leading to changes in fundamental biosynthetic processes (Fig. S4). Specifically, a significant number of RBPs (60 proteins) were differentially expressed, including members with known neuronal localization and involvement in neuronal functions, such as ELAV-1, ELAV-3, RBBP7, RNPS1, RNMT, TARDBP, XPO1, XPO5, HNRNPA1, HNRNPA1L2, HNRNPF, HNRNPL, HNRPNPM, HRNNPUL1, PABPC1, PABPC4, PTBP2 and CELF1 (Table S4). Since even small changes in RBP expression or activity are amplified due to their broad impact on

expression, splicing and translation of numerous RNA substrates, changes in such a large number of these RNA regulators suggest a severe perturbation in RNA homeostasis in p.A53T-neurons.

Of these p.A53T-affected RBPs, a cluster implicated in splicing and adenylation events in the nuclear compartment was restored after BX795 treatment (Fig. 4A). These RBPs included DEK, involved in splice site selection, RBM4, a modulator of alternative 5'-splice site and exon selection, MYEF2, an mRNA stabilizer, UBTF, a critical protein in rRNA transcription, SNRPB, a component of small RNPs essential for pre-mRNA splicing, PCBP1 that binds ssDNA sequences to guide mRNA splicing and regulators of transcription, ZNF207 and HINT1. RAE1, that acts as a major mRNA export factor and attaches cytoplasmic RNPs to the cytoskeleton, and HNRNPUL1 that belongs to the hnRNP family and has been linked to ALS due to its aggregation-prone motif, were also restored by BX795.

Pre-mRNA splicing determines nucleosome organization [35], whilst nucleosomes assembled around specific splice sites regulate transcription [36] . Nucleosome assembly was the major category of proteins downregulated in p.A53T-neurons (23 proteins) including histones 1.2, 1.3, 1.4, 1.5, H2A, H2B, H3.3 and H4, nuclear pore NUP153 and nuclear organizers Lamin-B1 and Prelamin A/C (Table S5). These downregulated proteins were not affected by BX795, whereas only the upregulated HIST1H1E and NUP93 that are important for nuclear pore complex assembly and maintenance, were restored by BX795 (Suppl. Table 3).

Protein Synthesis. Disturbances in RBP dosage have detrimental consequences also outside the nucleus, as they control the targeted localization of mRNAs, either proximally in the cell soma or distally in the projecting axon, affecting whether an mRNA will be translated or remain translationally silent and whether it will be stored for local mRNA translation or degraded [37]. Aberrant expression of the translational machinery emerged in the p.A53T proteome with translational initiation and regulation processes being the most affected in mutant neurons (Fig.

S4B, Table S4). A total of 18 proteins involved in the formation of the pre-initiation complex were identified and included EIF2, 3, 4 and 5, of which EIF4G2 that functions as a general suppressor of translation by forming translationally inactive stress granules, was targeted by BX795 (Fig. 4A). Ribosomal proteins (29 proteins), structural components of ribosome subunits, were upregulated in p.A53T-neurons (Table S4) and a significant fraction returned to near-control levels after BX795 treatment (Fig. 4A). These included RPL31 and RPL12, which are involved in 60S biogenesis, and RPS6, a component of the 40S subunit. tRNA processing represents another important part of the translational cascade that was altered in p.A53T-neurons (Table S4), while a significant fraction was restored by BX795 (Fig. 4A,Table S2). This included the aminoacyl-tRNA synthetases RARS (arginyl-tRNA synthase), VARS (valyl-tRNA synthase), and WARS (tryptophanyl-tRNA synthase), together with regulatory or accessory proteins such as PPA1, EEF1D (subunit of elongation factor-1 needed for enzymatic delivery of aminoacyl tRNAs to ribosome), PRMPT1 (arginine N-methyltransferase), FAM98B (a stimulator of PRMT-1 mediated arginine methylation) and RTCB (a catalytic subunit of the tRNA-splicing ligase complex). Although mutations in aminoacyl-tRNA synthetases have been implicated in various recessive and dominant disorders [38] and growing evidence associates changes in tRNA gene biogenesis and processing with neurodegenerative diseases [39], our data reveal for the first time a link between p.A53T-αSyn expression and this molecular process.

Protein modification and transport. p.A53T-αSyn toxicity has been attributed to problematic modifications at the ER membrane and disturbances in ER-Golgi and early endosomal/vesicle trafficking [29, 34, 40, 41]. In accordance, p.A53T-neurons exhibit altered protein levels in components of these pathways (Table S4). Among these, five members of the adaptor protein complexes that function in transport-vesicle mediated transfer between membranous structures are increased by p.A53T-expression: AP1B1, AP2A2, AP3B1, AP3D1 and AP3M1. Another

prominent category included members of the largest branch of Ras-like small GTPases involved in membrane trafficking, such as RAB2A, RAB2B and RAB6B, responsible for ER to Golgi transport; RAB18, important for early endosome formation as well as for macroautophagy, and strongly associated with neurodegeneration [42, 43]; and RAB21, regulator of integrin internalization and SNARE-mediated autophagosome-lysosome fusion [44]. Other dysregulated proteins involved in ER to Golgi trafficking included SEC22B and SEC31A whilst ARF1 and 3, two proteins required for vesicle budding/uncoating in the Golgi apparatus and required for synaptic stability of excitatory synapses [45] were also increased in p.A53T neurons (Table S4). Finally, another affected process seems to be the retrograde Golgi to ER transport, as coatomer proteins COPA, COPB, COPG were also dysregulated.

BX795 had a selective effect on p.A53T-altered transport proteins like SRP9, a signal recognition particle assembly molecule that targets proteins to RER membranes, GDI2, a regulator of RABs, CKAP4, a post-translational modifier, ATP6VOD1, part of a multi-subunit acidification enzyme required for protein sorting, the DAD1 subunit of oligosaccahryl transferase complex and OGT, both functioning at the initial steps of N-glycosylation, and NAPB, a SNAP protein with preferential expression in the brain involved in docking and fusion during ER to Golgi transfer (Fig. 4A). SAR1A, SEC22B and YKT6, all components of the SNARE complex, were also targeted by BX795 (Fig. 4A) whilst effects on molecules of the RAB, adaptor protein complex and coatomer remained largely unaffected.

Stress Response. p.A53T-αSyn protein expression acts as a primary neurotoxin triggering a battery of stress responses in human neurons [46]. The proteomics analysis indicated that p.A53T-neurons activate most of these mechanisms. Both the unfolded protein response (UPR), as evidenced by mis-expression of chaperones CCT2, 3, 4, 5, 7,and 8, as well as the heat shock

protein response (HSP), with proteins such as DNAJA1, DNAJB11, DNAJC7, HSPA4L, HSP9 and HSPE1, were apparent in the p.A53T-proteome (Table S4).

These stress response pathways were significantly downregulated in p.A53T neurons treated with BX795, which seems to target many of their mediators (Fig. 4A). These included TCP-1, a member of the chaperonin TCP1 complex (CCT) bearing a cavity where unfolded proteins enter to get properly folded, PTPN1, a tyrosine-protein phosphatase that acts as UPR regulator by EIF2AK3/PERK modulation, STIP1, a coordinator of HSP70 and HSP90 function, DNAJB11, a co-chaperone of HSPA5 that binds unfolded proteins-substrates for endoplasmic reticulum-associated degradation (ERAD), GCN1L1 a chaperone that activates the EIF2AK4/GCN2 ribosomal complex, the CCT8 part of the CCT chaperonin, and DNAJA1, a co-chaperone of HSP70.

Such a dysregulation of the UPR/HSP response systems in p.A53T neurons should result in the production of dangerous protein cargo and the formation of protein aggregates, as indeed identified by immunofluorescence (Fig. 2C). The p.A53T proteome also revealed alterations in protein clearance pathways with mediators of both proteasomal and autophagic systems being affected (Table S4). BX795 improved the expression of multiple ubiquitin-associated proteins suggesting partial restoration of proteasome targeting of aberrant protein products, in accordance with the decrease of protein aggregates in BX795-treated p.A53T neurons (Fig. 2C). BX795 restored the expression of PSMA3, a component of the 20S core proteasome complex that is essential for removing misfolded or damaged proteins and can also act in a ubiquitin-independent manner, UCHL1, a thiol protease involved in processing of ubiquitinated proteins, OTUB1, a highly specific Ub-isopeptidase that interacts with E3 ligases to edit polyubiquitin chain growth, PSME3, a subunit of the proteasome PA28-gamma regulator activated by DNA damage, CUL1, a core component of the SKP1-CUL1-F- box E3 ligase complex, PSMD12, component of the 26S proteasome, and UBA6, an activator of ubiquitin required for E2 ligase binding. VCP, an AAA

ATPase that extracts ubiquitinated proteins from large protein complexes for degradation and has been shown to co-localize with protein aggregates in various neurodegenerative diseases with proteasome inhibition, was another BX795-downregulated protein (Fig. 4A).

Additional components of the lysosomal pathway of autophagy targeted by BX795 included ATG4B, a member of the autophagy protein family required for vacuole transport during autophagy, PDCD6IP, a protein involved in multivesicular body (MVB) biogenesis and sorting of protein cargo of the MVB, AP3M1, an adaptor of AP3 complex that directs proteins from Golgi to lysosomes and DNM2, a microtubule protein involved in phagosome formation (Fig. 4A).

Finally, BX795 also modulated oxidative stress response mechanisms, as mitochondrial proteins were brought to near control levels. Such proteins included TOMM70A, a translocase of the outer membrane complex, MDH2, utilized in the NAD/NADH system and STOML2, a regulator of biosynthesis of mitochondria and stimulator of cardiolipin biosynthesis, a molecule recently shown to be associated with p.A53T neurotoxicity in human dopamine neurons [29].

STRING analysis of all 118 proteins affected by BX795 revealed a network with strong functional linkage among the majority of these proteins (Fig. 4B).

Proteins associated with neurodegeneration. An important measure of the biological significance of the proteomics profile of p.A53T neurons comes from comparisons with human genetic studies. Enrichment analysis for PD and other neurodegenerative diseases identified several proteins comprising both known and novel converging targets that were modified by BX795 (Fig. 5B). Among those, UCHL1/PARK5 has a variant possibly linked to lower susceptibility for PD, while a point mutation co-segregating with the disease has been identified in one family [47] and VPS35/PARK17-D620N mutated protein causes late-onset autosomal dominant PD [48]. FAM98B has been linked to SMA and ALS [49], VCP mutations can cause FTD, ALS and Charcot-Marie-Tooth diseases [50, 51], HINT1 autosomal recessive mutations lead to neuromytotonia and

axonal neuropathy [52], PAFAHB1 mutations and gene deletions lead to lissencephaly syndrome [53] and RBM4 is linked to Down's syndrome [54] (Fig. 5A, B). STRING analysis of the BX795-modified protein network to which αSyn was also incorporated, demonstrated a strong association between αSyn and 8 neurodegeneration-linked proteins (Fig. 5C).

These findings collectively deepen our understanding of p.A53T-mediated neurotoxicity and reveal key biological processes that are targeted by BX795 to alleviate p.A53T-αSyn-related phenotypes in human neurons.

BX795 affects the mTORC1 signaling pathway to attenuate protein synthesis and enhance autophagic flux in p.A53T-αSyn expressing cells

The p.A53T proteome clearly indicates aberrant mRNA translation and protein clearance mechanisms, both linked to mammalian aging and neurodegenerative diseases, that can be restored by BX795. The mammalian target of rapamycin (mTOR) signaling pathway is a central regulator of proteostasis and the p.A53T proteome clearly indicates hyperfunctional overactive biosynthetic processes that could be associated with alterations in mTORC1 activation. Components of this signaling cascade have emerged in the proteomics analysis of p.A53T-neurons, including RPS6, the major substrate of mTORC1, together with several RAG GTPases like IQGAP1, required for efficient activation of mTORC1, which were largely restored after BX795 treatment (Table S2). At the same time the positive reversal of protein degradation molecules by BX795, components of both the proteasome and autophagic systems as revealed by proteomics analysis, could be attributed to modulation of the mTORC1 pathway.

To validate whether BX795 has an effect on mTORC1 activity in p.A53T-αSyn expressing cells we transduced the human neuroblastoma cell line SH-SY5Y with a lentiviral vector for co-expression of the human p.A53T-αSyn together with the fluorescent protein DsRed for tracking the

transduced cells. Control cells were transduced with the same vector for expression of DsRed only. SH-SY5Y cells expressing the human p.A53T-αSyn displayed a prominent upregulation in the levels of phosphorylated RPS6 (p-RPS6) as compared to control cells 72h after transduction, whilst BX795 abolished this effect (Fig. 6A). The consequence of p-RPS6 activation through mTORC1 is an increase in mRNA translation and protein synthesis. Using a fluorescent assay to monitor global protein synthesis we observed a significant increase in p.A53T cells compared to control, while BX795 showed a strong potency in reversing the observed overactive protein synthesis (Fig. 6B). The effect of BX795 on the mTOR cascade was further verified in an inducible SH-SY5Y cell line that expresses the human p.A53T-αSyn upon withdrawal of Doxycycline (-Dox) (Fig. 6C) [55]. In this system, treatment with BX795 resulted in reduced levels of p-mTOR, p-PRAS40, a key component of the mTORC1 complex, and most prominently p-RPS6 (Fig. 6C), confirming the effect of this multi-kinase inhibitor in mRNA translation and protein synthesis pathways.

mTORC1 also controls autophagy, the major degradation pathway essential for removing macromolecules, including aggregation-prone αSyn [56, 57]. In particular, mTORC1 inhibition is linked to enhanced autophagy, therefore we examined if BX795 affects this clearance pathway. First, we monitored LC3-II protein, the processed form of LC3 that is associated with the abundance of autophagosomes and autolysosomes [58]. To this end we transfected the inducible SH-SY5Y cell line expressing p.A53T-αSyn (-Dox) with a fusion construct containing the green fluorescent protein tagged to LC3 (GFP-LC3), followed by confocal microscopy and quantification of GFP-LC3-II+ puncta comprising brightly fluorescent autophagosomes and more weakly labeled autolysosomes [59]. GFP-LC3-II+ puncta were barely detectable in control cells treated with DMSO. In the presence of BX795 alone there was a small, yet not significant increase in GFP-LC3-

II puncta (Fig. 6D) that became prominent in cells treated with bafilomycin, a blocker of autophagosome-lysosome fusion that prevents lysosome-mediated protein degradation (Fig 6D). Noticeably, the combination of bafilomycin and BX795 further increased the number and brightness of GFP-LC3-II puncta, suggesting that BX795 acts to induce autophagy (Fig 6D).

To distinguish labeled autophagosomes from autolysosomes in p.A53T-expressing SH-SY5Y cells and monitor autophagic flux, we used a dual fluorophore probe consisting of a tandem fluorescent mCherry-GFP-p62 construct [60]. p62 protein is a receptor for a ubiquitinated cargo destined to be degraded by autophagy and is associated with LC3-II within autophagosomes and autolysosomes [61]. As GFP fluorescence is sensitive to low pH, autophagosomes are double labeled with Cherry/GFP and appear as yellow puncta while autolysosomes within the same cell are labeled red with mCherry only. Quantification of yellow and red puncta revealed that the number of autophagosomes was significantly reduced in the presence of BX795 as compared to DMSO-treated cells while the number of autolysosomes showed a trend to increase albeit not significantly, suggesting that BX795 possibly facilitates the autophagic flux (Fig. 6E).

Overall this data show that BX795 clearly modulates protein synthesis and could facilitate autophagy clearance pathways.

Discussion

The generation of novel human models based on patient-derived iPSCs has opened up new perspectives for the investigation of disease mechanisms and the discovery of new therapeutics. In this work, we used a well-characterized human model of p.A53T pathology [18] to screen for small molecules with protective function. We thus identified the multi-kinase inhibitor BX795 as a compound that exerts a profound and sustainable beneficial effect on patient-derived p.A53T-neurons. Remarkably, we found that a single treatment with BX795 has long-lasting

consequences in supporting neuritic growth, limiting αSyn protein aggregate formation and restoring axonal neuropathology, recorded two weeks after its addition in human p.A53T neurons. Interestingly, the beneficial effects of BX795 were not restricted to dopaminergic neurons but had a more widespread effect on the p.A53T neuronal population.

To our knowledge, this study represents the first high-content drug discovery screen performed in human iPSC-derived neurons to identify candidate therapeutics for PD. Using an unbiased screening approach in combination with quantitative proteomics profiling, we were able to show that treatment with BX795 restored a cohort of 118 proteins out of the 648 proteins that are abnormally expressed in p.A53T-neurons. Restored proteins are associated with key cellular processes, most notably RNA metabolism, protein synthesis and degradation processes, as well as stress response, suggesting that restoration of proteostasis is key for rescuing the neuropathological features in p.A53T-neurons. Dissecting further the pathways affected by BX795 in the SH-SY5Y neuronal cell line expressing human p.A53T-αSyn, we demonstrated that BX795 modulates the mTORC1 pathway to restrict excessive protein synthesis and possibly facilitate autophagy. Taken together, our data highlight the BX795 kinase inhibitor as a promising compound and candidate therapeutic that ameliorates pathology in patient-derived p.A53T-neurons.

Considerable progress in understanding the neurotoxic properties of α-Syn has been achieved by exploiting causal mutations resulting in rare familial forms of PD, most notably the p.A53T-αSyn mutation (G209A in the *SNCA* gene) [62, 63]. We and others have shown that disease-associated characteristics can be recapitulated in patient-derived p.A53T-neurons including axonal degeneration and accumulation of protein inclusions resembling Lewy bodies and neurites [18]. These have been linked to multiple molecular defects in mRNA processing and translation, endocytic and retrograde trafficking [34, 41], protein misfolding, redox homeostasis [16, 29] and

the synaptic protein machinery [18]. The p.A53T proteome examined here revealed extensive alterations and a profound increase in proteins related to the biological processes of RNA metabolism, protein synthesis, modification and transport, protein clearance and stress response. Notably, the cohort of 118 proteins that was specifically restored in p.A53T-neurons upon treatment with BX795, was associated with these key cellular processes. Whether the dysregulated p.A53T proteome reflects cellular responses to αSyn-mediated pathology or causal defects associated with disease pathogenesis, is an interesting question that deserves further investigation. Nevertheless, the early neuronal differentiation stage at which our study was conducted argues in favor of causality rather than consequence, further illustrating the value of BX795 as potential therapeutic.

The pathways affected by mutant αSyn expression in our study have a high similarity with the αSyn connectome reported by Chung et al [34] for mouse neurons, and the *in silico* "humanized" map of αSyn proteotoxicity predicted for human neurons in the accompanying study of Khurana et al [41]. Our proteomics analysis, the first accomplished in p.A53T-human neurons, identified perturbations in RNA metabolic processes that started from the nucleus and reached the ribosome. Among these, dysregulation of RBPs that has been linked to aggregation processes and the formation of stress granules in multiple neurodegenerative disorders is very prominent [64-67]. RBPs act throughout the biological cycle of mRNA processing [68] and their function can be divided into nuclear and cytoplasmic events. In the p.A53T-proteome, proteins involved in mRNA splicing, elongation and export from the nucleus were significantly upregulated, indicating that a re-organization of nucleosomal components occurs within the nucleus, regulating splicing site accessibility [35, 69]. Nucleosome assembly components were largely downregulated in p.A53T-neurons but all 24 proteins in this group were not affected by BX795 and remained at abnormally low levels compared to control. Looking at these categories collectively along with

the strong nuclear component depicted by cellular component enrichment, we speculate that p.A53T-αSyn may affect nuclear processes through its suspected role as a DNA-binding protein or DNA-damage response modulator [70-72].

Alternative mRNA processing greatly increases the dimensions of gene expression through splicing, polyadenylation, targeted localization and post-transcriptional silencing. Neurons take advantage of all these strategies as the brain has the highest levels of alternative splicing compared to any other human tissue [73]. This process has recently been shown to be defective in the PS19 Tau model of Alzheimer's disease, where enhanced TIA-mediated alternative splicing events were shown to affect genes particularly involved in synaptic transmission [74]. Similarly, the p.A53T-proteome suggests that this process could be excessively induced in p.A53T-neurons as a number of RBPs known to be linked to αSyn aggregation have emerged, including ELAV1, ELAV3 and CELF, suggesting a possible association with the abnormal expression of synaptic genes and the defective synaptic connectivity we have previously observed in p.A53T neurons-[18].

An excess of mRNAs coming out of the nucleus in p.A53T-neurons could explain the abnormal expression of proteins involved in translation, the next step of mRNA processing. Indeed, the significant increase of components of the tRNA splicing ligase complex, various aminoacyl-tRNA synthetases, ribosomal subunits and eukaryotic translation initiation factors indicate an enhanced translation of spliced mRNAs. Aberrant protein synthesis has been reported in p.A53T-derived neurons, but in the opposite direction by Khurana et al [41] that might reflect differences in maturation stage. In our study, we have analyzed p.A53T-neurons at a relatively early stage, when they are still able to direct mRNA species to the ribosome for translation, instead of forming stress granules where translationally silent mRNAs are contained.

The mTOR kinase is a master regulator of cellular metabolism that functions in two distinct complexes: mTORC1 and mTORC2 [75] with the first implicated in protein and lipid biosynthesis through a signaling cascade that includes SK6 and 4E-BP1 proteins [76]. Unlike proliferating cells where this pathway is utilized for growth and division, in neurons it acts as a regulator of healthy metabolism and aging [77] with its restriction being associated with prolonged life span and delay of age-related pathologies. p.A53T-neurons have increased RPS6, IQGAP1 and RAG-GTPases, components of mTORC1 pathway and this seems to be associated with an increased translation of a subset of mRNAs that are linked to RNA metabolism and the stress response. Similarly, a quantitative proteomics study of a presymptomatic p.A53T-αSyn Drosophila model shows significant upregulation of ribosomal proteins in the p.A53T flies [78]. In agreement, expression of human p.A53T-αSyn in the neuronal cell line SH-SY5Y resulted in increased global protein synthesis mediated by mTORC1 that was strongly inhibited by BX795 (Fig. 6). Although the mechanistic link between αSyn and mTORC1 remains to be established, recent evidence shows that genetic variability in the mTOR pathway contributes to SNCA effects in disease pathogenesis [79].

Concomitantly with promoting protein synthesis mTORC1 acts to repress autophagy through ULK1 phosphorylation. Autophagy has a central role in promoting health and longevity by removal of toxic material such as damaged organelles and large protein aggregates while this process is impaired in neurodegenerative diseases and αSyn pathology [80, 81]. The p.A53T-proteome shows that neurons are under stress as proteins involved in the UPR or the heat-shock stress response, proteasome assembly and regulation, known to be orchestrated by mTORC1 in neurons, are significantly upregulated [77]. Accumulation of unfolded or misfolded proteins in p.A53T-neurons, including a large portion of RBPs that have an intrinsic propensity to aggregate, would result in misregulation of the autophagic system. Indeed, electron microscopic

observations in p.A53T-neurons have revealed abnormal accumulation of autophagosomes identified as multiple multilamellar bodies engulfing subcellular organelles, that were never seen in control cells (our unpublished observations). Similar findings have been identified in p.A53T αSyn-expressing PC12 cells [82] Restoration of numerous components of RNA metabolism and protein translation cascades by BX795 is directly related to the diminished stress response that emerges by the lower levels of UPR and heat-shock-associated proteins also conferred by this molecule. In parallel, a significant number of ubiquitin/proteasome-associated proteins were brought back to near control levels. Considering that both the ubiquitin/proteasome system and autophagy share multiple molecular determinants, including ULK1, ATG5, ATG8 and p62, which can be simultaneously and mutually affected in neurodegenerative diseases [83, 84], it becomes evident that BX795 helps misfolded protein clearance by limiting protein synthesis. This is in agreement with its demonstrated ability to decrease protein aggregates in p.A53T-neurons, as shown in this study, along with facilitation of autophagy in SYSH-5Y cells expressing p.A53T.

BX795 is a multi-kinase inhibitor that targets numerous pathways, including the kinases TBK1 and PDK1 [26-28, 31]. Although in our system differences in the total or phosphorylated levels of these two kinases were not observed in the presence of BX795 (data not shown), we cannot exclude that its neuroprotective effects are mediated through these two kinases as both are involved in neurodegeneration, mTOR signaling and autophagy [85, 86]. Yet four other PDK1 inhibitors that were included in the Selleck library did not emerge as hits during the screening campaign. TBK1 was recently suggested as a new player linking autophagy and neuroinflammation in ALS [85] and has been shown to activate mTOR directly in response to growth factors [87]. In agreement, we demonstrated an acute effect of BX795 in mTOR, RPS6 and PRAS40 phosphorylation in p.A53T-expressing neuroblastoma cells. Noticeably multiple other inhibitors of mTOR phosphorylation (26 in total, including rapamycin) were components of the

kinase inhibitor library tested, but failed to show any protective effects, implying that BX795 might act indirectly in this pathway. Considering that BX795 has been proposed to act through distinct mechanisms in different pathologies, future mechanistic studies should reveal its direct targets in p.A53T neurons. Nevertheless, the work presented here uniquely identifies BX795 as a promising compound that may have therapeutic potential for patients with PD and other protein conformational disorders. Further, our collective data along with previous proteomics and systems approaches shed light into the molecular and cellular pathways of αSyn proteotoxicity unveiling new disease targets for the development of combined therapeutics.

Materials and Methods

Directed neuronal differentiation. iPSCs used in this study were previously generated and characterized from two Parkinson's disease patients harboring the p.A53T-α-synuclein mutation and a healthy subject (control, wild-type SNCA) as previously described [18]. For directed differentiation, iPSCs were allowed to form embryoid bodies and neural induction was initiated by applying a dual SMAD inhibition protocol in the presence of Noggin and TGFβ inhibitor for generation of neural precursor cells (NPCs) [18]. NPCs were maintained and expanded in DMEM/F12/B27/N2-medium supplemented with HEPES, Glutamax, non-essential amino acids [NEAA] and 20ug/ml FGF2. For neuronal differentiation, NPCs were dissociated with accutase and seeded onto poly-L-ornithine (20 µg/ml; Sigma-Aldrich)/laminin (5 µg/ml; Sigma-Aldrich)-coated 35mm dishes in DMEM/F12/ B27/N2-medium supplemented with 200 ng/ml human recombinant sonic hedgehog (SHH, R&D Systems) and 100 ng/ml murine recombinant fibroblast growth factor 8b (FGF-8b, R&D Systems) for 7 days in vitro (DIV). On 7 DIV cells were dissociated with accutase and seeded onto poly-L-ornithine/ laminin-coated plates in DMEM/F12/B27/N2-medium supplemented with 20 ng/ml brain-derived neurotrophic factor (BDNF, R&D Systems), 20 ng/ml glial cell-derived neurotrophic factor (GDNF, R&D Systems), 200 µM ascorbic acid (AA, Sigma-Aldrich) and 0.5 mM cyclic AMP (cAMP, Sigma- Aldrich). The medium was changed every 2 to 3 days for 2 weeks.

Compound screening and analysis. For high content screening, iPSC-derived NPCs at 7 DIV were dissociated with accutase and were seeded (9,000 cells/well) onto poly-L-ornithine/ laminin-coated 384-well optical bottom plates containing the kinase inhibitors (Greiner Bio-One, Kremsmünster, Austria) in DMEM/F12/B27/N2-medium supplemented with 20 ng/ml BDNF/GDNF/AA/cAMP as described above (Fig. 1A). The medium was changed every 2 to 3 days for 2 weeks. A collection of 273 small molecule kinase inhibitors from Selleck Chemicals was used

in this study. The list of molecules and their known targets according to the provider is shown in Table S1. Two week prior imaging the cells, the compounds were dispensed in duplicate in 384-well optical bottom plates at a final concentration of 1μM. After 2 weeks of neuronal maturation the cells were fixed in 4% paraformaldehyde (PFA) for 20 min followed by immunofluorescence staining for βIII-tubulin (TUJ1) and Tyrosine hydroxylase (TH) at 4°C overnight, followed by incubation with appropriate secondary antibodies (Molecular Probes, Thermo Fisher Scientific) conjugated to AlexaFluor 488 (green) or 546 (red), for at least 1 h at room temperature. Nuclei were stained with Hoechst dye. Images per well were captured by automated confocal microscopy (Opera High-Content Screening System, Perkin Elmer, Hamburg, Germany). To quantify the fluorescence and texture of our images, we used Image Mining, a custom-made image processing and analysis application with an extendable "plug-in" infrastructure [88]. A total of 15 images per well were acquired using a 10X magnifying objective and analyzed with Image Mining software. The number of cell nuclei and fluorescence staining of cells were quantified by segmentation on 15 images per well in a duplicate experimental setup.

RNA isolation, cDNA Synthesis and qRT-PCR. Total RNA was extracted from cell pellets using the TRIzol® Reagent (Life Technologies). Following digestion with DNaseI, 1 μg of total RNA was used for first strand cDNA synthesis with the ImProm-II Reverse Transcription System (Promega) according to the manufacturer's instructions. Quantitative RT-PCR analyses were carried out in a Light Cycler 96 (Roche). Real time PCR detection system using KAPA SYBR FAST qPCR Master Mix (KapaBiosystems). All primers used are listed in Table S6.

Immunofluorescence staining. Cells were fixed with 4% paraformaldehyde (Sigma-Aldrich) for 20 min at room temperature. Samples were blocked with 0.1% Triton X-100 (Sigma-Aldrich) and 5% donkey serum in PBS for 30 min and were subsequently incubated with primary antibodies (Table S6) at 4°C overnight, followed by incubation with appropriate secondary antibodies

(Molecular Probes, Thermo Fisher Scientific) conjugated to AlexaFluor 488 (green) or 546 (red), for at least 1 h at room temperature. Protein aggregates were detected with the PROTEOSTAT Aggresome Detection Kit (Enzo) followed by immunolabeling for TUJ1 [18, 19]Coverslips were mounted with ProLong Gold antifade reagent with DAPI (Cell Signaling) and images were acquired using a Leica TCSSP5II confocal microscope (LEICA Microsystems) and analyzed using ImageJ software (NIH).

Neurite analysis. Neurite analysis was performed on iPSC-derived neurons at 21 DIV. Immunofluorescence staining was performed for Tyrosine Hydroxylase (TH). The number of neurites extending from the soma of at least 50 single TH^+ neurons per sample was determined. Neurite length was estimated by manually tracing the length of all neurites on TH-labeled neurons using the NeuronJ plugin of ImageJ (NIH).

Axon degeneration index. Analysis of axon degeneration was performed by immunostaining for βIII-tubulin (TUJ1) in iPSC-derived PD neuronal cultures. The cultures were either untreated (in the presence of DMSO) or treated with BX795. The number of TUJ1+ spots in blebbed or fragmented axons was counted manually (ImageJ) on twenty randomly selected fields and the ratio between the number of spots and the total TUJ1+ staining area (ImageJ) was defined as axon degeneration index.

Proteomic Analysis. iPSC-derived neurons at 21 DIV were suspended, lysed and the proteins reduced in 4% SDS, 100 mM DTT, 100 mM Tris pH 7.8 through heating for 5 min. Next, the proteins were alkylated by 100 mM iodoacetamide treatment for 30 min in the dark. Samples were further processed according to the Single-Pot Solid-Phase enhanced Sample Preparation (SP3) method of Hughes et al. Digestion was carried out overnight at 37°C using Trypsin/LysC mix (Promega) at a protein/enzyme ratio of 50:1 in a ThermoMixer under continuous mixing at 1000 rpm. After digestion, the tubes were placed on a magnetic rack, and the supernatant containing

the peptides was collected and dried down in a centrifugal evaporator (Savant SPD 1010, Thermo scientific). The peptide mixtures were reconstituted in a solution of 2% (v/v) ACN and 0.1% (v/v) formic acid. The peptide solution was incubated for 3 min in a sonication water bath. Peptide concentration was determined by nanodrop absorbance measurement at 280 nm.

Ultra high pressure nanoLC. 2.5 µg peptides were pre-concentrated with a flow of 3 µL/min for 10 min using a C18 trap column (Acclaim PepMap100, 100 µm x 2 cm, Thermo Scientific) and then loaded onto a 50 cm long C18 column (75 µm ID, particle size 2 µm, 100Å, Acclaim PepMap100 RSLC, Thermo Scientific). The binary pumps of the HPLC (RSLCnano, Thermo Scientific) consisted of Solution A (2% (v/v) ACN in 0.1% (v/v) formic acid) and Solution B (80% (v/v) ACN in 0.1% (v/v) formic acid). The peptides were separated using a linear gradient of 4% B up to 40% B in 340 min with a flow rate of 300 nL/min. The column was placed in an oven operating at 35°C.

LC-MS/MS. The eluted peptides were ionized by a nanospray source and detected by an LTQ Orbitrap XL mass spectrometer (Thermo Fisher Scientific, Waltham, MA, USA) operating in a data dependent mode (DDA). Full scan MS spectra were acquired in the orbitrap (m/z 300–1600) in profile mode with the resolution set to 60,000 at m/z 400 and automatic gain control target at 106 ions. The six most intense ions were sequentially isolated for collision-induced (CID) MS/MS fragmentation and detection in the linear ion trap. Dynamic exclusion was set to 1 min and activated for 90 sec. Ions with single charge states were excluded. Lockmass of m/z 445,120025 was used for continuous internal calibration. XCalibur (Thermo Scientific) was used to control the system and acquire the raw files.

Protein identification and quantification. The mass spectral files (raw files) were processed using MaxQuant software (version 1.6.9.0). Default parameters were used for protein identification and quantification. Trypsin specificity was set to allow two missed cleavages and minimum

peptide length was set to 7 amino acids. Cysteine carbamidomethylation was set as fixed, and methionine oxidation, deamidation of asparagine and glutamine and N-terminal acetylation were set as variable modifications. A maximum of 5 modifications per peptide was set. The false discovery rate both for peptide and protein was set to 1%. For calculation of protein abundances, label-free quantification (LFQ) was performed with both "second peptides" and "match between run" options enabled. The human FASTA files were from UniProt downloaded on 15 October 2019.

Proteomic data analysis. Statistical analysis was performed using Perseus (1.6.6.0). Proteins identified as contaminants, "reverse" and "only identified by site" were filtered out. The LFQ intensities were transformed to logarithmic values [log2(x)]. The protein groups were filtered to obtain at least 2 valid values in at least one group. The label-free quantified proteins were subjected to statistical analysis with ANOVA test (permutation based p-value with 0.05 cutoff). LC-MS/MS data after statistical analysis were plotted in a volcano graph based on the difference between the two samples expressed as log2(x) versus their statistical significance expressed as –Log10(p-value). Hierarchical clustering was carried out on Z-score transformed LFQ values using average linkage of Euclidian distance. GO Enrichment analysis for biological processes, molecular function and cellular compartment was performed using DAVID functional annotation tools with official gene symbol as identifiers, the Homo sapiens background and the GOTERM_DIRECT annotation categories. A P value of 0.05 was selected as the cutoff criterion. The enrichment of proteins involved in signaling pathways was performed using the Reactome pathway database. A P value of 0.01 was selected as the cutoff criterion.

Western blot. iPSC-derived neurons or SH-SY5Y cell cultures were lysed at 4^{o}C for 15 min in ice cold lysis buffer [150mMNaCl, 50 mM Tris (pH 7.5), 1%v/v Triton X-100, 1mM EDTA, 1mM EGTA, 0.1% SDS, 0.5% Nsodium deoxycholate containing PhosSTOP phosphatase inhibitors and a

complete protease inhibitor mixture (Roche Life Science), and centrifuged at 20,000 g. Protein concentration was estimated in the supernatant by Bradford assay (Applichem). Proteins were separated by SDS-polyacrylamide gel electrophoresis (PAGE) and transferred onto nitrocellulose membranes (Maine Manufacturing). For phospho-(Ser129)-αSyn detection, the membrane was heated at 65 ^{0}C overnight in PBS. Nonspecific binding sites were blocked in TBS/ 0.1% Tween 20/5% skimmed milk for 1 hour at 20°C ^{0}C followed by overnight incubation with primary antibodies diluted in TBS/0.1% Tween20/3% BSA or in TBS/0.1% Tween 20/5% skimmed milk. Incubation with appropriate HRP-conjugated secondary antibodies (Thermo) was performed for 2 hours at room temperature and protein bands were visualized using the Clarity Western ECL Substrate (BIO-RAD).

Production of CMV.DsRed and CMV.DsRed.A53T lentiviral vectors. Four plasmids were used for lentivirus generation: the lentiviral transfer vector and three lentiviral packaging vectors (pMDL, pRev and pVSVG; provided by Dr. Fred Gage, the Salk Institute for Biological Studies). The lentiviral transfer vectors for expression of either the red fluorescent protein DsRed under the control of CMV promoter (LV.CMV.DsRed) or for co-expression of the red fluorescent protein DsRed, a T2A bicistronic configuration and p.A53T-αSyn under the control of CMV promoter (LV.CMV.DsRed.T2A.A53T) were constructed by VectorBuilder. The preparation and purification of the lentiviral vectors were performed as previously described (Tiscornia G, Singer O, & Verma IM (2006) Production and purification of lentiviral vectors. Nat Protoc 1(1):241-245.)**.** LV.CMV.DsRed and LV.CMV.DsRed.T2A.A53T were used for transduction of the human neuroblastoma cell line SH-SY5Y that was routinely maintained in regular RPMI 1640 medium (Gibco) supplemented with 10% FBS (Gibco) and 1% penicillin/streptomycin (Life Technologies) at 37°C in a humidified atmosphere containing 5% CO2 and 95% air.

Protein synthesis assay. For detection of total protein synthesis an assay Kit (ab239725) (Abcam) was used that utilizes a cell permeable analog of puromycin, O-Propargyl-puromycin which, once inside the cell, stops translation by forming covalent conjugates with nascent polypeptide chains. Truncated polypeptides are rapidly turned over by the proteasome and can be detected based on a click reaction with fluorescent azide. SH-SY5Y cells transduced with either the control vector LV.CMV.DsRed or LV.CMV.DsRed.T2A.A53T for expression of p.A53T-αSyn were pre-treated with DMSO vehicle or BX795 for 24h and were incubated for 2h with fresh aliquots of media containing either Protein Label or Protein Label and BX795. Cells were then fixed with 4% paraformaldehyde (Sigma-Aldrich) for 20 min at room temperature. Coverslips were mounted with ProLong Gold antifade reagent with DAPI (Cell Signaling) and images were acquired using a Leica TCSSP5II confocal microscope (LEICA Microsystems) and analyzed using ImageJ software (NIH).

Cell culture and transfection of the inducible SH-SY5Y line. The inducible SH-SY5Y cell line expressing human p.A53T-αSyn was created and characterized as previously described [55]. It was maintained in regular RPMI 1640 (Gibco) supplemented with 10% FBS (Gibco) and 1% penicillin/streptomycin (Life Technologies) at 37°C in a humidified atmosphere containing 5% CO2 and 95% air. The expression of p.A53T-αSyn was switched off by the addition of doxycycline (Dox) (2 μg/mL). Transfection with the GFP-LC3 and mChery-GFP-p62 plasmids (a kind gift from Dr Tamotsu Yoshimori, Osaka University, Japan and Dr Terje Johansen, University of Tromso, Norway, respectively) was performed in the absence of Dox using Lipofectamine 2000 transfection reagent, according to the manufacturer's protocol (Invitrogen; Thermo Fisher Scientific, Inc.).

Statistics. All experiments were replicated at least three times and data from parallel cultures were acquired. All data represent mean ± standard error of the mean (SEM). Statistical analysis was performed using GraphPad Prism 6 software. Statistical significance was calculated for two

groups using Student's t-tests or the Mann-Whitney test for non-parametric distribution. Group comparisons of data were performed by one-way ANOVA test. P-values < 0.05 were considered significant; *p < 0.05, **p < 0.01, ***p < 0.001, ****p<0.0001.

Figure Legends

Fig 1: Identification of BX795 by high content screening of a kinase inhibitor library

A. Directed differentiation of Pax6+ (green)/ Nestin+ (red) neural precursor cells (NPCs; DIV 0, left) into TUJ1+ (red)/ TH+ (green) neurons (DIV 21, right). The differentiation protocol and timeline of analysis are shown in the drawing in the middle. The 273 kinase inhibitors were added at DIV 7 and image acquisition was performed at DIV 21. FG2 and FGF8, fibroblast growth factors 2 and 8; SHH, Sonic Hedgehog; AA, ascorbic acid; Scale bar represents BDNF, brain-derived neurotrophic factor; GDNF, glial cell-derived neurotrophic factor (GDNF); cAMP, cyclic AMP. Scale bars, 50 µm.

B. Scatter plot showing the ratio of TH versus Tuj1 expression in duplicate upon drug treatment with 273 small kinase molecule inhibitors. The dots inside the green square correspond to the 4 hit compounds show significant increase TH versus Tuj1 expression ratio as compared to the DMSO controls (blue dots). The red arrow indicates BX795.

C. Representative images of p.A53T-neurons immunolabelled for TH in 384-well plates. Upper micrograph shows control DMSO-treated cells while lower micrograph represents BX795-treated cells. Scale bar represents 150 µm.

D. Tests of the four hit compounds in a dose-response format. Data are presented as mean ± SEM.

Fig 2: Rescue of neuropathological features in p.A53T neurons by BX795

A. BX795 has a positive effect on neurite length of p.A53T-neurons. Representative confocal images of p.A53T-neurons immunostained for TH and quantification of total neurite length of TH+ cells. Data represent mean ± SEM. (*t*-test *P<0.05, n=4 independent experiments with at least 50 cells analyzed in each experiment). Scale bar, 50µm.

B. BX795 alleviates axonal neuropathology in p.A53T-neurons as demonstrated by immunostaining for βIII-tubulin (TUJ1; confocal images). Higher magnification at the right (upper, DMSO-treated cells; lower, BX795-treated cells) shows neurites with swollen varicosities or fragmented processes (arrows). Scale bar, 30µm. Quantification of axonal degeneration is estimated in the accompanying graph by measuring the ratio of TUJ1+ spots over the total TUJ1+ area in untreated (DMSO) or BX795-treated p.A53T-neurons. Data represent mean ± SEM. (*t*-test, *P< 0.05, n = 20 randomly selected fields for each condition).

C. BX795 reduces protein aggregates in p.A53T-neurons. Representative confocal images showing protein aggregates in TUJ1+ cells (Scale bar, 10µm) and quantification in untreated (DMSO) or BX795-treated TUJ1+ cells (Mann–Whitney test; DMSO median 3.00, n=83 cells; BX795 median 3.00, n=93 cells; *P< 0.05).

D. Detection and quantification of p(Ser129)αSyn by Western blot (WB); Actin shows equal protein loading. Data represent mean ± SEM (t-test, *P<0.05, n=4 independent experiments).

Fig 3: Bioinformatics analysis of dysregulated proteins in p.A53T-neurons that are restored by BX795.

A. Hierarchical clustering of 118 upregulated proteins in p.A53T-neurons that are restored upon treatment with BX795 (one-way ANOVA analysis). Columns in the different groups (control, p.A53T-neurons and p.A53T-neurons treated with BX795) correspond to individual samples tested and rows represent single proteins (blue, low expression; red, high expression; n=3 for control and p.A53T; n=2 for p.A53T+BX795).

B. GO enrichment analysis for biological processes, molecular function and cellular compartments was performed using DAVID software (p<0.01).

C. Pathway analysis using Reactome software (p<0.01)

Fig 4: Protein network of pathways and processes restored by BX795 treatment

A. Heatmaps illustrating specific proteins upregulated in p.A53T-neurons that are involved in RNA metabolism, protein synthesis, protein transport and modification and response to stress and are restored after BX795 treatment. High expression is in red and low expression is in blue.

B. STRING-analysis representation of the protein-protein interaction network of the 118 upregulated proteins in p.A53T-neurons that are restored by BX795. Each circular node depicts one protein and the different colors represent the different pathways/processes as indicated. Connecting lines represent protein-protein associations and line intensity represents the confidence score of a functional association.

Fig 5: Restoration of disease-associated proteins by BX795 in p.A53T-neurons

A. Heatmap of proteins associated with neurodegeneration that are restored after BX795 treatment. High expression is in red and low expression is in blue.

B. Disease-associated proteins that are modified by BX795 are either known or associated genetic risk factors for neurodegenerative diseases as revealed by human genetic studies.

C. STRING network analysis of the neurodegeneration-associated proteins restored by BX795 in p.A53T-neurons and their interaction with αSyn. Each αSyn interactor is shown as a colored circle and connecting lines between proteins represent protein-protein associations. The intensity of lines represents the confidence score of a functional association.

Fig 6: BX795 affects the mTORC1 signaling pathway to attenuate protein synthesis and facilitate autophagy

A. Upregulation of pRPS6 levels in SH-SY5Y cells transduced to express human p.A53T-αSyn and re-establishment to control levels by BX795, as determined by immunofluorescence. Representative confocal images showing transfected SH-SY5Y cells (red) with a control vector for DsRed expression or the same vector for co-expression of p.A53T-αSyn and DsRed, immunolabeled for pRPS6 (green). Nuclei are visualized with Hoechst (blue). The quantification graph shows green fluorescence intensity [arbitrary units (A.U)] in transfected cells. Data represent mean ± SEM, ****p<0.0001, n= 38 cells for DsRed, n=41 cells for p.A53T, n=41 for p.A53T+BX795).

B. Assessment of global protein synthesis and quantification of fluorescence intensity in control and human p.A53T-αSyn expressing SH-SY5Y cells in the absence or presence of BX795. Representative confocal images showing transfected SH-SY5Y cells with control (DsRed) or p.A53T-αSyn/DsRed expressing vector using a fluorescent assay. Transfected cells are depicted in red and protein synthesis is in green. Nuclei are visualized with Hoechst (blue). Data represent mean ± SEM (*t*-test, *P < 0.05, ****P < 0.0001, n=at least 160 cells per condition).

C. Western blot showing an acute reduction in the levels of p-mTOR, p-PRAS40 and p-RPS6 in the inducible SH-SY5Y cell line (-Dox) expressing the human p.A53T-αSyn, in the presence of BX795. Actin shows equal protein loading. Data represent mean ± SEM (*t*-test, *P<0.05, ** P<0.01, n=3 independent experiments).

D. Assessment of autophagic flux in the inducible SH-SY5Y cell line expressing p.A53T-αSyn (-Dox). Representative confocal images of individual cells transfected with GFP-LC3 that were treated or not with BX795 in the presence or absence of bafilomycin A1, and quantification of GFP+ puncta/cell (Mann–Whitney Test; DMSO median 5.00, n=72 cells; BX795 median 5.00, n=79 cells; DMSO/Bafilomycin A1 median 56.00, n=69 cells; BX795/Bafilomycin A1 median 77.5, n=70 *P < 0.05).

E. Assessment of autophagic flux in the inducible SH-SY5Y cell line expressing p.A53T-αSyn (-Dox). Representative confocal images of individual cells transfected with GFP-mCherry-p62 that were treated with or without BX795 and quantification of yellow (autophagosomes) and red (autolysosomes) puncta/cell (Mann–Whitney Test; DMSO autophagosomes median 12.00, n=90 cells; BX795 autophagosomes median 10.00, n=82 cells; DMSO autolysosomes median 38.00, n=90 cells; BX795 autolysosomes A1 median 36.5, n=82 cells **P < 0.01).

Supplementary Figures

Fig S1: Expression of dopaminergic markers in p.A53T-iPSC-derived neurons

A. RTqPCR analysis of selected domaminergic markers in iPSC-derived neurons at 21 DIV: Tyrosine Hydrosylase (TH), Nuclear receptor related 1 protein (Nurr1) and Aromatic L-amino acid decarboxylase (AADC) normalized to GAPDH levels. Data represent mean ± SEM (n = 3)

B. (Left) Immunostaining of iPSC-derived neurons at 21 DIV. Cells were stained (red) for ki67. Hoechst+ nuclei are in blue. (Scale bar, 50 µm). (Right) Quantification of ki67+ cells. Data represent mean ± SEM (n = 3).

C. (Left) Immunostaining of iPSC-derived neurons at 21 DIV. Cells were stained (green) for Nestin and TH and (red) for βIIItubulin (TUJ1). Hoechst+ nuclei are in blue. (Scale bar, 50 µm) (Right) Quantification of Nestin+, TH+ and TUJ1 cells. Data represent mean ± SEM (n = 3).

Fig S2: Identification of toxic compounds in the small molecule library of kinase inhibitors

Summary of total nuclei counts from two screening plates. Compounds in cells with low nuclei counts were considered toxic and where excluded from the analysis. Each assay plate was normalized to DMSO.

Fig S3: Rescue of neuropathological features by BX795 in p.A53T neurons from a second patient

A. BX795 has a positive effect on neurite length of p.A53T-neurons. Representative confocal images of p.A53T-neurons immunostained for TH and quantification of total neurite length of TH+ cells. Data represent mean ± SEM. (n=at least 50-60 cells per condition from two independent experiments). Scale bar, 50µm.

B. BX795 alleviates axonal neuropathology in p.A53T-neurons as demonstrated by immunostaining for βIII-tubulin (TUJ1; confocal images). Neurites with swollen varicosities or fragmented processes are indicated with arrows. Scale bar, 30µm. Quantification of axonal degeneration is estimated in the accompanying graph by measuring the ratio of TUJ1+ spots over the total TUJ1+ area in untreated (DMSO) or BX795-treated p.A53T-neurons. Data represent mean ± SEM.

Fig S4: Identification of the biological processes that are dysregulated in p.A53T neurons

A. Volcano plot of differentially expressed proteins between control and p.A53T-neurons assessed by quantitative proteomics analysis. Each point represents the difference in expression (fold-change) between the two groups plotted against the level of statistical significance. Blue dots correspond to proteins downregulated in p.A53T neurons while red dots show proteins upregulated in p.A53T neurons (FDR=0.05, S0 = 0.1, as indicated by black lines).

B. GO enrichment analysis for biological processes of the differentially expressed proteins was performed using DAVID software ($p<0.05$).

List of Tables and their headings

Table S1: Kinase Inhibitor Library (Selleck Chemicals) and targets

Table S2: List of the 118 dysregulated proteins in p.A53T neurons that were restored upon treatment with BX795

Table S3: GO analysis for cellular compartment between pA53T and control neurons

Table S4: Differentially expressed proteins between pA53T and control neurons

Table S5: Nucleosome assembly proteins

Table S6: Primary antibodies and primers used in the current study

References

1. Baker, M.G. and L. Graham, *The journey: Parkinson's disease.* BMJ, 2004. **329**(7466): p. 611-4.
2. Olanow, C.W. and W.G. Tatton, *Etiology and pathogenesis of Parkinson's disease.* Annu Rev Neurosci, 1999. **22**: p. 123-44.
3. Pfeiffer, R.F., *Non-motor symptoms in Parkinson's disease.* Parkinsonism Relat Disord, 2016. **22 Suppl 1**: p. S119-22.
4. Gibb, W., *Idiopathic Parkinson's disease and the Lewy body disorders.* Neuropathology and applied neurobiology, 1986. **12**(3): p. 223-234.
5. Lewandowsky, M.H., *Handbuch der neurologie: bd. Spezielle Neurologie IV*. Vol. 5. 1914: J. Spring.
6. Chartier-Harlin, M.C., et al., *Alpha-synuclein locus duplication as a cause of familial Parkinson's disease.* Lancet, 2004. **364**(9440): p. 1167-9.
7. Petrucci, S., M. Ginevrino, and E.M. Valente, *Phenotypic spectrum of alpha-synuclein mutations: New insights from patients and cellular models.* Parkinsonism Relat Disord, 2016. **22 Suppl 1**: p. S16-20.
8. Simon-Sanchez, J., et al., *Genome-wide association study reveals genetic risk underlying Parkinson's disease.* Nat Genet, 2009. **41**(12): p. 1308-12.
9. Cotzias, G.C., M.H. Van Woert, and L.M. Schiffer, *Aromatic amino acids and modification of parkinsonism.* N Engl J Med, 1967. **276**(7): p. 374-9.
10. Baba, M., et al., *Aggregation of alpha-synuclein in Lewy bodies of sporadic Parkinson's disease and dementia with Lewy bodies.* Am J Pathol, 1998. **152**(4): p. 879-84.
11. Ghosh, D., et al., *alpha-synuclein aggregation and its modulation.* Int J Biol Macromol, 2017. **100**: p. 37-54.
12. Ghosh, D., et al., *The Parkinson's disease-associated H50Q mutation accelerates alpha-Synuclein aggregation in vitro.* Biochemistry, 2013. **52**(40): p. 6925-7.
13. Schulz-Schaeffer, W.J., *The synaptic pathology of alpha-synuclein aggregation in dementia with Lewy bodies, Parkinson's disease and Parkinson's disease dementia.* Acta Neuropathol, 2010. **120**(2): p. 131-43.
14. Chen, M., et al., *Common proteomic profiles of induced pluripotent stem cell-derived three-dimensional neurons and brain tissue from Alzheimer patients.* J Proteomics, 2018. **182**: p. 21-33.
15. Cooper, O., et al., *Pharmacological rescue of mitochondrial deficits in iPSC-derived neural cells from patients with familial Parkinson's disease.* Sci Transl Med, 2012. **4**(141): p. 141ra90.
16. Ryan, S.D., et al., *Isogenic human iPSC Parkinson's model shows nitrosative stress-induced dysfunction in MEF2-PGC1alpha transcription.* Cell, 2013. **155**(6): p. 1351-64.
17. Yang, Y.M., et al., *A small molecule screen in stem-cell-derived motor neurons identifies a kinase inhibitor as a candidate therapeutic for ALS.* Cell Stem Cell, 2013. **12**(6): p. 713-26.
18. Kouroupi, G., et al., *Defective synaptic connectivity and axonal neuropathology in a human iPSC-based model of familial Parkinson's disease.* Proc Natl Acad Sci U S A, 2017. **114**(18): p. E3679-E3688.
19. Zygogianni, O., et al., *In Vivo Phenotyping of Familial Parkinson's Disease with Human Induced Pluripotent Stem Cells: A Proof-of-Concept Study.* Neurochem Res, 2019. **44**(6): p. 1475-1493.
20. Chambers, S.M., et al., *Highly efficient neural conversion of human ES and iPS cells by dual inhibition of SMAD signaling.* Nat Biotechnol, 2009. **27**(3): p. 275-80.
21. Soldner, F., et al., *Parkinson's disease patient-derived induced pluripotent stem cells free of viral reprogramming factors.* Cell, 2009. **136**(5): p. 964-77.
22. Lovestone, S., et al., *A phase II trial of tideglusib in Alzheimer's disease.* J Alzheimers Dis, 2015. **45**(1): p. 75-88.
23. Pagan, F.L., et al., *Pharmacokinetics and pharmacodynamics of a single dose Nilotinib in individuals with Parkinson's disease.* Pharmacol Res Perspect, 2019. **7**(2): p. e00470.
24. Cuny, G.D., *Kinase inhibitors as potential therapeutics for acute and chronic neurodegenerative conditions.* Curr Pharm Des, 2009. **15**(34): p. 3919-39.
25. Yu, T., et al., *The kinase inhibitor BX795 suppresses the inflammatory response via multiple kinases.* Biochem Pharmacol, 2020. **174**: p. 113797.

26. Clark, K., et al., *Use of the pharmacological inhibitor BX795 to study the regulation and physiological roles of TBK1 and IkappaB kinase epsilon: a distinct upstream kinase mediates Ser-172 phosphorylation and activation.* J Biol Chem, 2009. **284**(21): p. 14136-46.
27. Jaishankar, D., et al., *An off-target effect of BX795 blocks herpes simplex virus type 1 infection of the eye.* Sci Transl Med, 2018. **10**(428).
28. Su, A.R., et al., *BX-795 inhibits HSV-1 and HSV-2 replication by blocking the JNK/p38 pathways without interfering with PDK1 activity in host cells.* Acta Pharmacol Sin, 2017. **38**(3): p. 402-414.
29. Ryan, T., et al., *Cardiolipin exposure on the outer mitochondrial membrane modulates alpha-synuclein.* Nat Commun, 2018. **9**(1): p. 817.
30. Walker, D.G., et al., *Changes in properties of serine 129 phosphorylated alpha-synuclein with progression of Lewy-type histopathology in human brains.* Exp Neurol, 2013. **240**: p. 190-204.
31. Bai, L.Y., et al., *BX795, a TBK1 inhibitor, exhibits antitumor activity in human oral squamous cell carcinoma through apoptosis induction and mitotic phase arrest.* Eur J Pharmacol, 2015. **769**: p. 287-96.
32. Cox, J., et al., *Accurate proteome-wide label-free quantification by delayed normalization and maximal peptide ratio extraction, termed MaxLFQ.* Mol Cell Proteomics, 2014. **13**(9): p. 2513-26.
33. Cox, J. and M. Mann, *MaxQuant enables high peptide identification rates, individualized p.p.b.-range mass accuracies and proteome-wide protein quantification.* Nat Biotechnol, 2008. **26**(12): p. 1367-72.
34. Chung, C.Y., et al., *In Situ Peroxidase Labeling and Mass-Spectrometry Connects Alpha-Synuclein Directly to Endocytic Trafficking and mRNA Metabolism in Neurons.* Cell Syst, 2017. **4**(2): p. 242-250 e4.
35. Keren-Shaul, H., G. Lev-Maor, and G. Ast, *Pre-mRNA splicing is a determinant of nucleosome organization.* PLoS One, 2013. **8**(1): p. e53506.
36. Chen, W., L. Luo, and L. Zhang, *The organization of nucleosomes around splice sites.* Nucleic Acids Res, 2010. **38**(9): p. 2788-98.
37. Bowden, H.A. and D. Dormann, *Altered mRNP granule dynamics in FTLD pathogenesis.* J Neurochem, 2016. **138 Suppl 1**: p. 112-33.
38. Park, S.G., P. Schimmel, and S. Kim, *Aminoacyl tRNA synthetases and their connections to disease.* Proc Natl Acad Sci U S A, 2008. **105**(32): p. 11043-9.
39. Kapur, M., C.E. Monaghan, and S.L. Ackerman, *Regulation of mRNA Translation in Neurons-A Matter of Life and Death.* Neuron, 2017. **96**(3): p. 616-637.
40. Chung, C.Y., et al., *Identification and rescue of alpha-synuclein toxicity in Parkinson patient-derived neurons.* Science, 2013. **342**(6161): p. 983-7.
41. Khurana, V., et al., *Genome-Scale Networks Link Neurodegenerative Disease Genes to alpha-Synuclein through Specific Molecular Pathways.* Cell Syst, 2017. **4**(2): p. 157-170 e14.
42. Carpanini, S.M., et al., *A novel mouse model of Warburg Micro syndrome reveals roles for RAB18 in eye development and organisation of the neuronal cytoskeleton.* Dis Model Mech, 2014. **7**(6): p. 711-22.
43. Feldmann, A., et al., *The RAB GTPase RAB18 modulates macroautophagy and proteostasis.* Biochem Biophys Res Commun, 2017. **486**(3): p. 738-743.
44. Jean, S., et al., *Starvation-induced MTMR13 and RAB21 activity regulates VAMP8 to promote autophagosome-lysosome fusion.* EMBO Rep, 2015. **16**(3): p. 297-311.
45. Rocca, D.L., et al., *The small GTPase Arf1 modulates Arp2/3-mediated actin polymerization via PICK1 to regulate synaptic plasticity.* Neuron, 2013. **79**(2): p. 293-307.
46. Farley, M.M. and T.A. Watkins, *Intrinsic Neuronal Stress Response Pathways in Injury and Disease.* Annu Rev Pathol, 2018. **13**: p. 93-116.
47. Maraganore, D.M., et al., *UCHL1 is a Parkinson's disease susceptibility gene.* Ann Neurol, 2004. **55**(4): p. 512-21.
48. Williams, E.T., X. Chen, and D.J. Moore, *VPS35, the Retromer Complex and Parkinson's Disease.* J Parkinsons Dis, 2017. **7**(2): p. 219-233.
49. Chi, B., et al., *The neurodegenerative diseases ALS and SMA are linked at the molecular level via the ASC-1 complex.* Nucleic Acids Res, 2018. **46**(22): p. 11939-11951.

50. Abramzon, Y.A., et al., *The Overlapping Genetics of Amyotrophic Lateral Sclerosis and Frontotemporal Dementia.* Front Neurosci, 2020. **14**: p. 42.
51. Gonzalez, M.A., et al., *A novel mutation in VCP causes Charcot-Marie-Tooth Type 2 disease.* Brain, 2014. **137**(Pt 11): p. 2897-902.
52. Aminkeng, F., *HINT1 mutations define a novel disease entity - autosomal recessive axonal neuropathy with neuromyotonia.* Clin Genet, 2013. **83**(1): p. 31-2.
53. Haverfield, E.V., et al., *Intragenic deletions and duplications of the LIS1 and DCX genes: a major disease-causing mechanism in lissencephaly and subcortical band heterotopia.* Eur J Hum Genet, 2009. **17**(7): p. 911-8.
54. Bernert, G., M. Fountoulakis, and G. Lubec, *Manifold decreased protein levels of matrin 3, reduced motor protein HMP and hlark in fetal Down's syndrome brain.* Proteomics, 2002. **2**(12): p. 1752-7.
55. Xilouri, M., et al., *Abberant alpha-synuclein confers toxicity to neurons in part through inhibition of chaperone-mediated autophagy.* PLoS One, 2009. **4**(5): p. e5515.
56. Parekh, P., et al., *A Cleaning Crew: The Pursuit of Autophagy in Parkinson's Disease.* ACS Chem Neurosci, 2019. **10**(9): p. 3914-3926.
57. Rabanal-Ruiz, Y., E.G. Otten, and V.I. Korolchuk, *mTORC1 as the main gateway to autophagy.* Essays Biochem, 2017. **61**(6): p. 565-584.
58. Kabeya, Y., et al., *LC3, a mammalian homologue of yeast Apg8p, is localized in autophagosome membranes after processing.* EMBO J, 2000. **19**(21): p. 5720-8.
59. Lopez, A., A. Fleming, and D.C. Rubinsztein, *Seeing is believing: methods to monitor vertebrate autophagy in vivo.* Open Biol, 2018. **8**(10).
60. Pankiv, S., et al., *p62/SQSTM1 binds directly to Atg8/LC3 to facilitate degradation of ubiquitinated protein aggregates by autophagy.* J Biol Chem, 2007. **282**(33): p. 24131-45.
61. Jiang, P. and N. Mizushima, *LC3- and p62-based biochemical methods for the analysis of autophagy progression in mammalian cells.* Methods, 2015. **75**: p. 13-8.
62. Spira, P.J., et al., *Clinical and pathological features of a Parkinsonian syndrome in a family with an Ala53Thr alpha-synuclein mutation.* Ann Neurol, 2001. **49**(3): p. 313-9.
63. Yamaguchi, K., et al., *Abundant neuritic inclusions and microvacuolar changes in a case of diffuse Lewy body disease with the A53T mutation in the alpha-synuclein gene.* Acta Neuropathol, 2005. **110**(3): p. 298-305.
64. Apicco, D.J., et al., *Reducing the RNA binding protein TIA1 protects against tau-mediated neurodegeneration in vivo.* Nat Neurosci, 2018. **21**(1): p. 72-80.
65. Brunello, C.A., X. Yan, and H.J. Huttunen, *Internalized Tau sensitizes cells to stress by promoting formation and stability of stress granules.* Sci Rep, 2016. **6**: p. 30498.
66. De Santis, R., et al., *Mutant FUS and ELAVL4 (HuD) Aberrant Crosstalk in Amyotrophic Lateral Sclerosis.* Cell Rep, 2019. **27**(13): p. 3818-3831 e5.
67. Martinez, F.J., et al., *Protein-RNA Networks Regulated by Normal and ALS-Associated Mutant HNRNPA2B1 in the Nervous System.* Neuron, 2016. **92**(4): p. 780-795.
68. Wolozin, B., *Regulated protein aggregation: stress granules and neurodegeneration.* Mol Neurodegener, 2012. **7**: p. 56.
69. Naftelberg, S., et al., *Regulation of alternative splicing through coupling with transcription and chromatin structure.* Annu Rev Biochem, 2015. **84**: p. 165-98.
70. Milanese, C., et al., *Activation of the DNA damage response in vivo in synucleinopathy models of Parkinson's disease.* Cell Death Dis, 2018. **9**(8): p. 818.
71. Pinho, R., et al., *Nuclear localization and phosphorylation modulate pathological effects of alpha-synuclein.* Hum Mol Genet, 2019. **28**(1): p. 31-50.
72. Schaser, A.J., et al., *Alpha-synuclein is a DNA binding protein that modulates DNA repair with implications for Lewy body disorders.* Sci Rep, 2019. **9**(1): p. 10919.
73. Yeo, G., et al., *Variation in alternative splicing across human tissues.* Genome Biol, 2004. **5**(10): p. R74.
74. Apicco, D.J., et al., *Dysregulation of RNA Splicing in Tauopathies.* Cell Rep, 2019. **29**(13): p. 4377-4388 e4.

75. Johnson, S.C., P.S. Rabinovitch, and M. Kaeberlein, *mTOR is a key modulator of ageing and age-related disease.* Nature, 2013. **493**(7432): p. 338-45.
76. Kim, J. and K.L. Guan, *mTOR as a central hub of nutrient signalling and cell growth.* Nat Cell Biol, 2019. **21**(1): p. 63-71.
77. Papadopoli, D., et al., *mTOR as a central regulator of lifespan and aging.* F1000Res, 2019. **8**.
78. Xun, Z., et al., *Quantitative proteomics of a presymptomatic A53T alpha-synuclein Drosophila model of Parkinson disease.* Mol Cell Proteomics, 2008. **7**(7): p. 1191-203.
79. Fernandez-Santiago, R., et al., *SNCA and mTOR Pathway Single Nucleotide Polymorphisms Interact to Modulate the Age at Onset of Parkinson's Disease.* Mov Disord, 2019. **34**(9): p. 1333-1344.
80. Arotcarena, M.L., M. Teil, and B. Dehay, *Autophagy in Synucleinopathy: The Overwhelmed and Defective Machinery.* Cells, 2019. **8**(6).
81. Menzies, F.M., et al., *Autophagy and Neurodegeneration: Pathogenic Mechanisms and Therapeutic Opportunities.* Neuron, 2017. **93**(5): p. 1015-1034.
82. Stefanis, L., et al., *Expression of A53T mutant but not wild-type alpha-synuclein in PC12 cells induces alterations of the ubiquitin-dependent degradation system, loss of dopamine release, and autophagic cell death.* J Neurosci, 2001. **21**(24): p. 9549-60.
83. Levine, B. and G. Kroemer, *Biological Functions of Autophagy Genes: A Disease Perspective.* Cell, 2019. **176**(1-2): p. 11-42.
84. Pohl, C. and I. Dikic, *Cellular quality control by the ubiquitin-proteasome system and autophagy.* Science, 2019. **366**(6467): p. 818-822.
85. Oakes, J.A., M.C. Davies, and M.O. Collins, *TBK1: a new player in ALS linking autophagy and neuroinflammation.* Mol Brain, 2017. **10**(1): p. 5.
86. Pietri, M., et al., *PDK1 decreases TACE-mediated alpha-secretase activity and promotes disease progression in prion and Alzheimer's diseases.* Nat Med, 2013. **19**(9): p. 1124-31.
87. Bodur, C., et al., *The IKK-related kinase TBK1 activates mTORC1 directly in response to growth factors and innate immune agonists.* 2018. **37**(1): p. 19-38.
88. Dorval, T., et al., *Contextual automated 3D analysis of subcellular organelles adapted to high-content screening.* J Biomol Screen, 2010. **15**(7): p. 847-57.

Figure 1

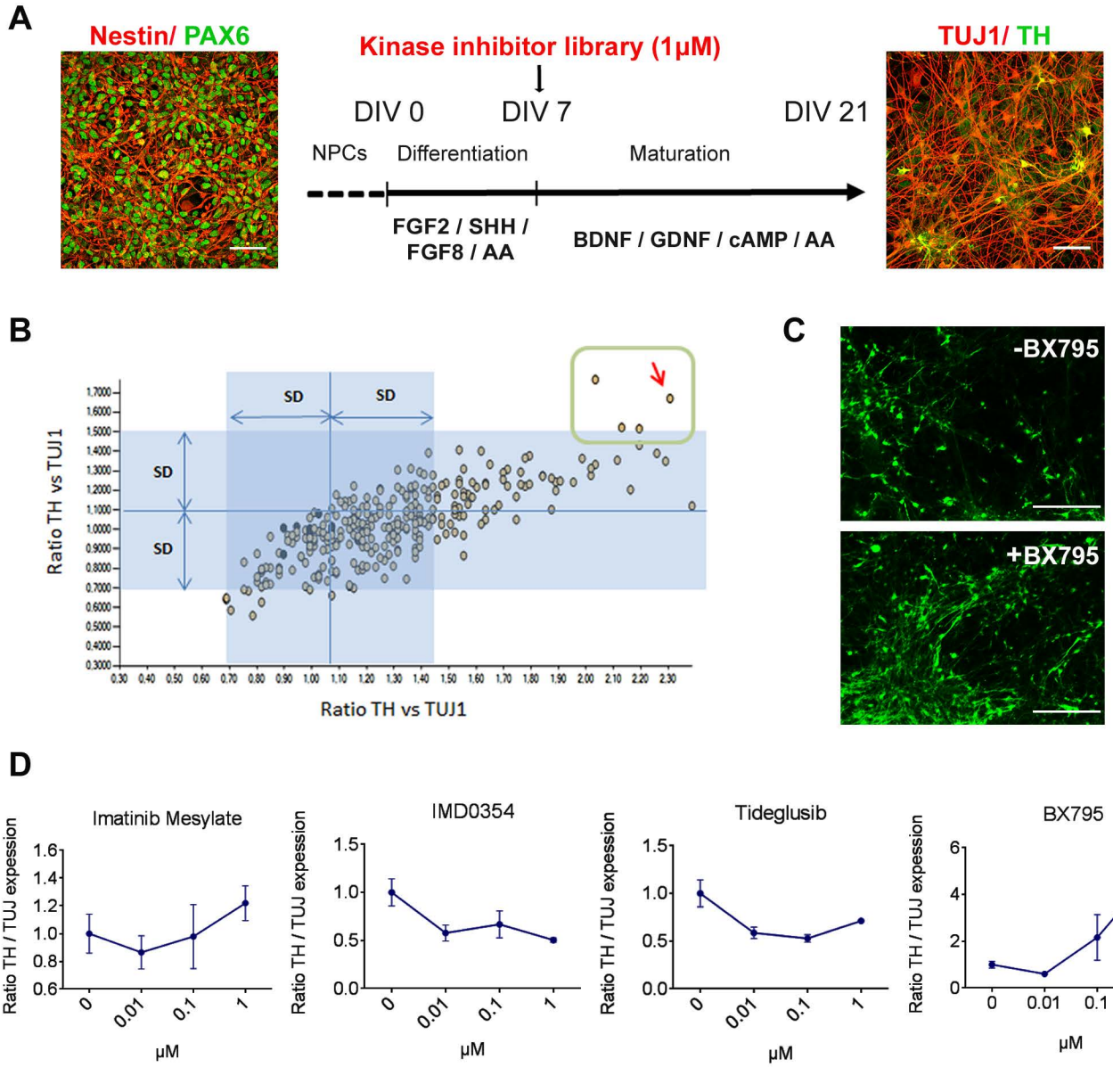
A
Nestin/ PAX6
Kinase inhibitor library (1μM)
DIV 0
DIV 7
DIV 21
NPCs
Differentiation
Maturation
FGF2 / SHH /
FGF8 / AA
BDNF / GDNF / cAMP / AA
TUJ1/ TH
B
SD
SD
SD
SD
Ratio TH vs TUJ1
Ratio TH vs TUJ1
C
-BX795
+BX795
D
Imatinib Mesylate
IMD0354
Tideglusib
BX795
Ratio TH / TUJ expression
μM

Figure 2

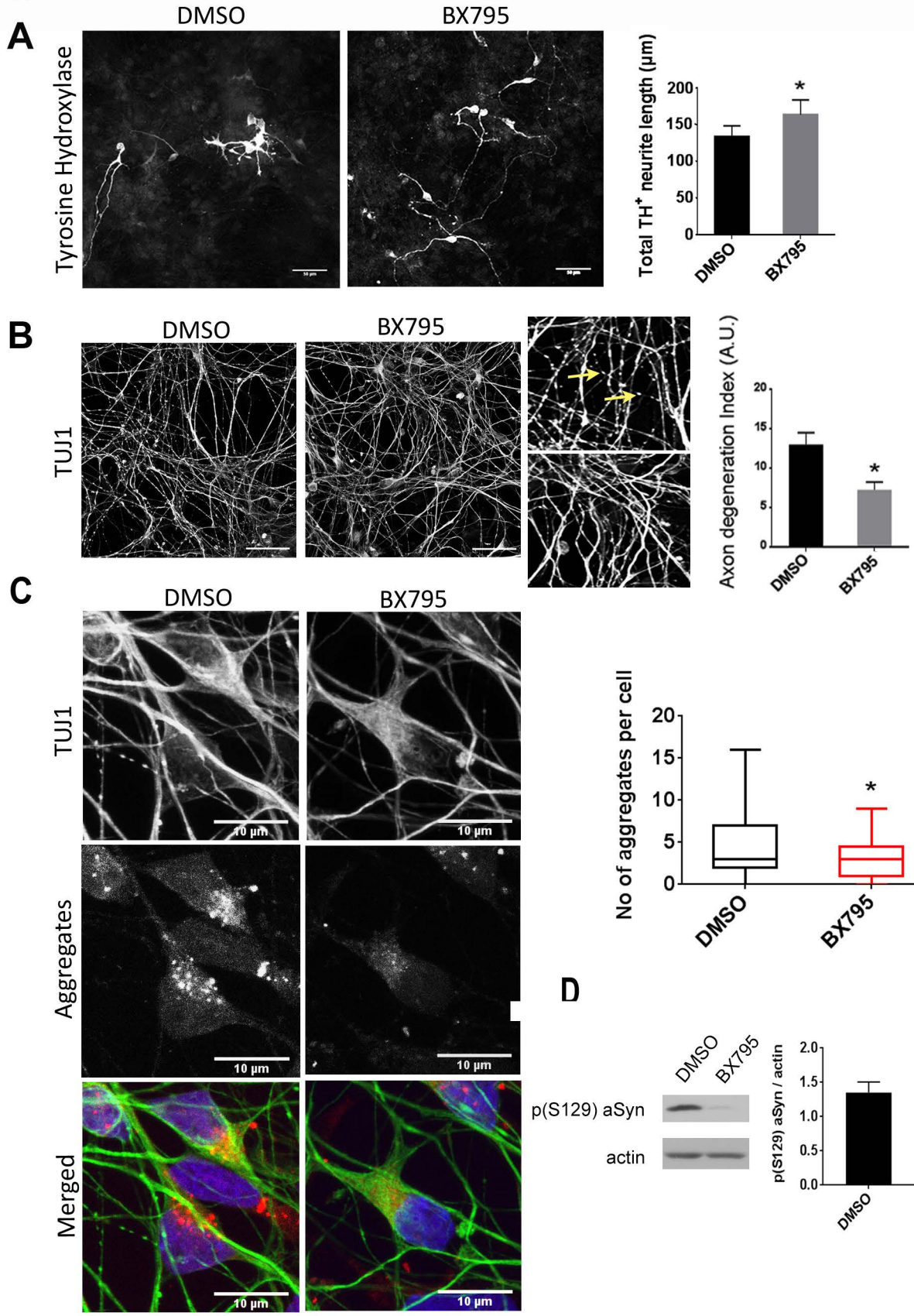
A
DMSO
BX795
Tyrosine Hydroxylase
Total TH+ neurite length (µm)
200
150
100
50
0
*
DMSO
BX795
B
DMSO
BX795
TUJ1
Axon degeneration Index (A.U.)
20
15
10
5
0
*
DMSO
BX795
C
DMSO
BX795
TUJ1
Aggregates
Merged
10 µm
No of aggregates per cell
20
15
10
5
0
*
DMSO
BX795
D
DMSO
BX795
p(S129) aSyn
actin
p(S129) aSyn / actin
2.0
1.5
1.0
0.5
0.0
*
DMSO
BX795

Figure 3

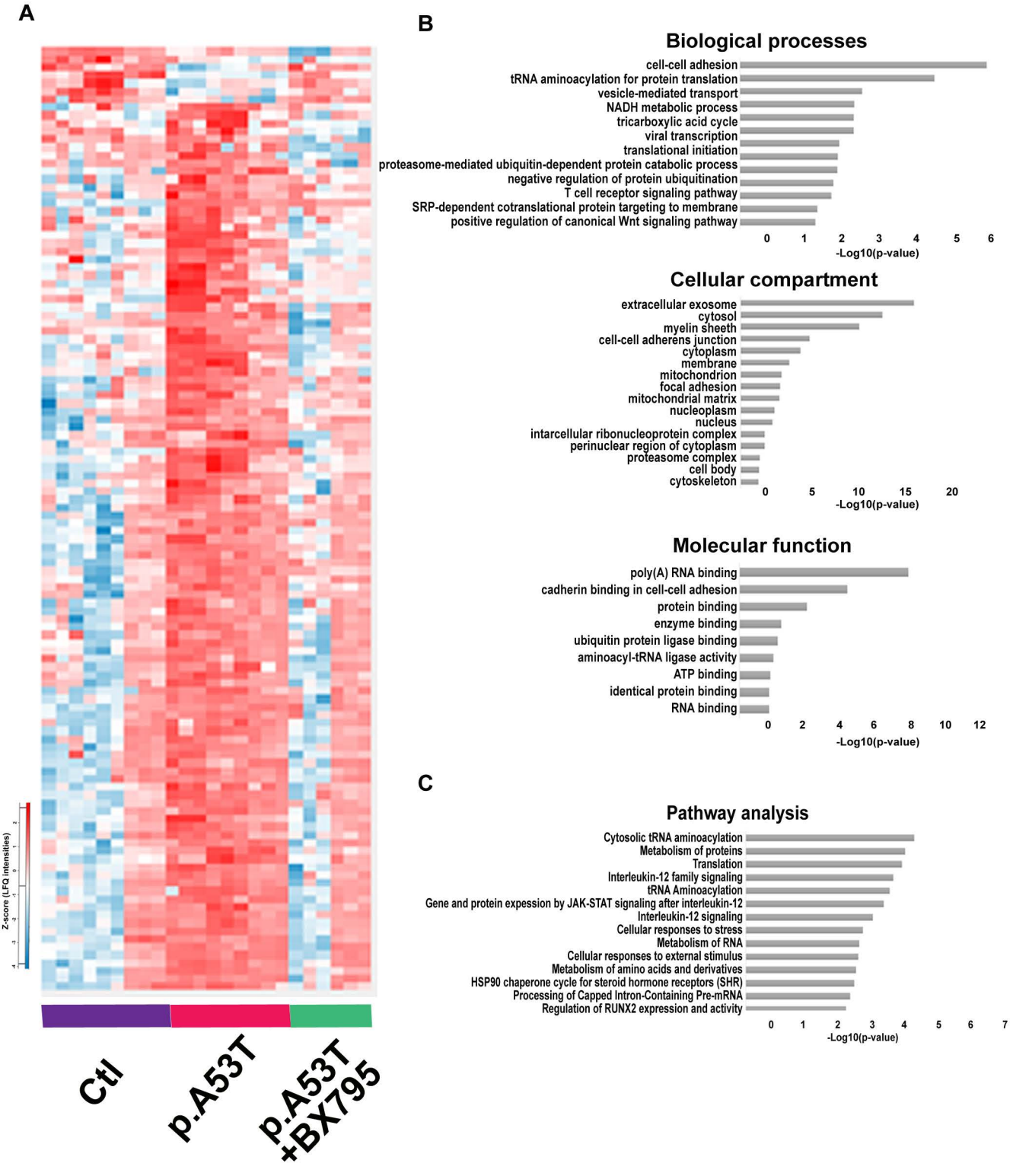
A
Z-score (LFQ intensities)
Ctl
p.A53T
p.A53T +BX795
B
Biological processes
cell-cell adhesion
tRNA aminoacylation for protein translation
vesicle-mediated transport
NADH metabolic process
tricarboxylic acid cycle
viral transcription
translational initiation
proteasome-mediated ubiquitin-dependent protein catabolic process
negative regulation of protein ubiquitination
T cell receptor signaling pathway
SRP-dependent cotranslational protein targeting to membrane
positive regulation of canonical Wnt signaling pathway
0 1 2 3 4 5 6
-Log10(p-value)
Cellular compartment
extracellular exosome
cytosol
myelin sheeth
cell-cell adherens junction
cytoplasm
membrane
mitochondrion
focal adhesion
mitochondrial matrix
nucleoplasm
nucleus
intarcellular ribonucleoprotein complex
perinuclear region of cytoplasm
proteasome complex
cell body
cytoskeleton
0 5 10 15 20
-Log10(p-value)
Molecular function
poly(A) RNA binding
cadherin binding in cell-cell adhesion
protein binding
enzyme binding
ubiquitin protein ligase binding
aminoacyl-tRNA ligase activity
ATP binding
identical protein binding
RNA binding
0 2 4 6 8 10 12
-Log10(p-value)
C
Pathway analysis
Cytosolic tRNA aminoacylation
Metabolism of proteins
Translation
Interleukin-12 family signaling
tRNA Aminoacylation
Gene and protein expession by JAK-STAT signaling after interleukin-12
Interleukin-12 signaling
Cellular responses to stress
Metabolism of RNA
Cellular responses to external stimulus
Metabolism of amino acids and derivatives
HSP90 chaperone cycle for steroid hormone receptors (SHR)
Processing of Capped Intron-Containing Pre-mRNA
Regulation of RUNX2 expression and activity
0 1 2 3 4 5 6 7
-Log10(p-value)

Figure 4

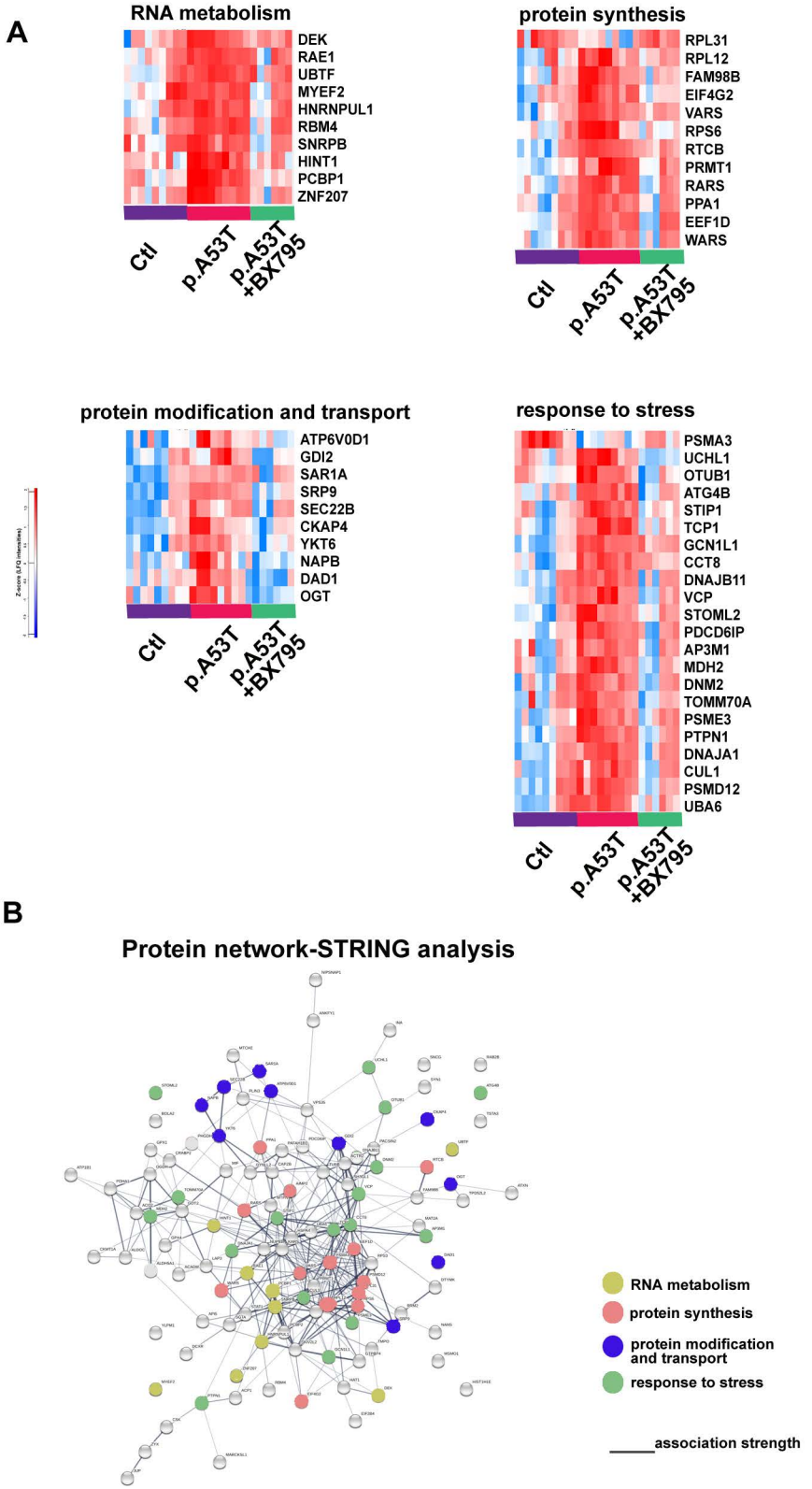
A
RNA metabolism
DEK
RAE1
UBTF
MYEF2
HNRNPUL1
RBM4
SNRPB
HINT1
PCBP1
ZNF207
Ctl
p.A53T
p.A53T +BX795
protein synthesis
RPL31
RPL12
FAM98B
EIF4G2
VARS
RPS6
RTCB
PRMT1
RARS
PPA1
EEF1D
WARS
Ctl
p.A53T
p.A53T +BX795
protein modification and transport
ATP6V0D1
GDI2
SAR1A
SRP9
SEC22B
CKAP4
YKT6
NAPB
DAD1
OGT
Ctl
p.A53T
p.A53T +BX795
response to stress
PSMA3
UCHL1
OTUB1
ATG4B
STIP1
TCP1
GCN1L1
CCT8
DNAJB11
VCP
STOML2
PDCD6IP
AP3M1
MDH2
DNM2
TOMM70A
PSME3
PTPN1
DNAJA1
CUL1
PSMD12
UBA6
Ctl
p.A53T
p.A53T +BX795
B
Protein network-STRING analysis
RNA metabolism
protein synthesis
protein modification and transport
response to stress
association strength

Figure 5

A

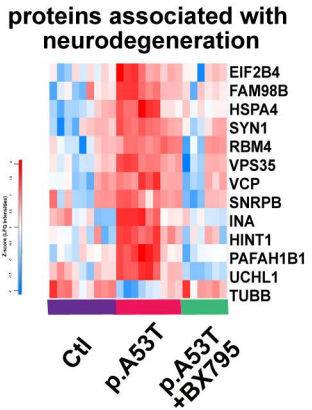
proteins associated with neurodegeneration
EIF2B4
FAM98B
HSPA4
SYN1
RBM4
VPS35
VCP
SNRPB
INA
HINT1
PAFAH1B1
UCHL1
TUBB
Ctl
p.A53T
p.A53T +BX795

B

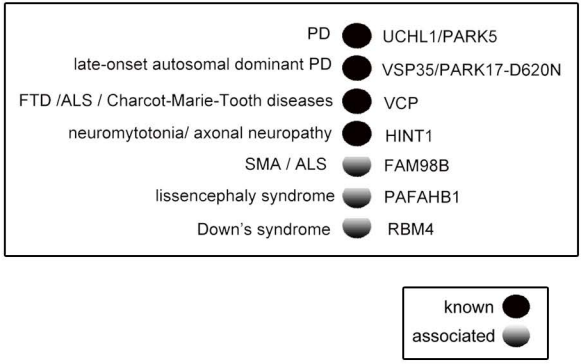
PD
UCHL1/PARK5
late-onset autosomal dominant PD
VSP35/PARK17-D620N
FTD /ALS / Charcot-Marie-Tooth diseases
VCP
neuromytotonia/ axonal neuropathy
HINT1
SMA / ALS
FAM98B
lissencephaly syndrome
PAFAHB1
Down's syndrome
RBM4
known
associated

C

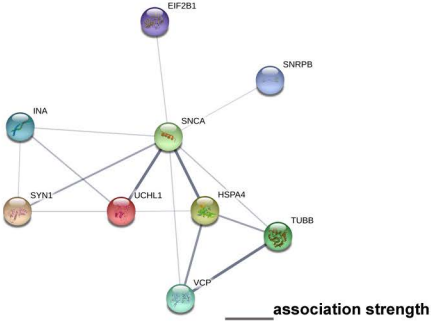
EIF2B1
SNRPB
INA
SNCA
SYN1
UCHL1
HSPA4
TUBB
VCP
association strength

Figure 6

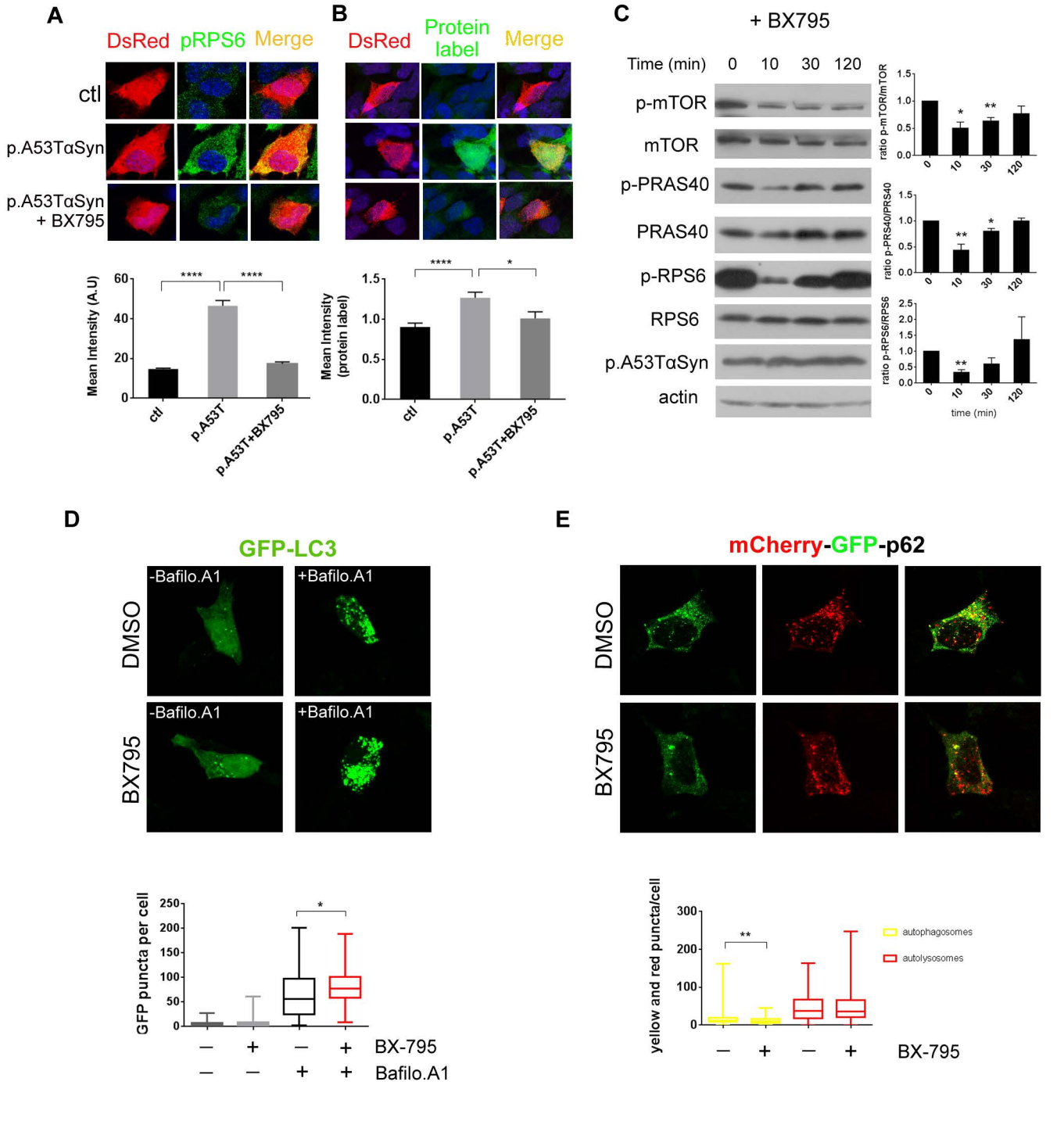
A
DsRed
pRPS6
Merge
ctl
p.A53TαSyn
p.A53TαSyn + BX795
Mean Intensity (A.U)
ctl
p.A53T
p.A53T+BX795
B
DsRed
Protein label
Merge
Mean Intensity (protein label)
C
+ BX795
Time (min)
p-mTOR
mTOR
p-PRAS40
PRAS40
p-RPS6
RPS6
p.A53TαSyn
actin
ratio p-mTOR/mTOR
ratio p-PRS40/PRS40
ratio p-RPS6/RPS6
time (min)
D
GFP-LC3
-Bafilo.A1
+Bafilo.A1
DMSO
BX795
GFP puncta per cell
BX-795
Bafilo.A1
E
mCherry-GFP-p62
yellow and red puncta/cell
autophagosomes
autolysosomes